# Endothelial proteolytic activity and interaction with non-resorbing osteoclasts mediate bone elongation

Sara G. Romeo[1,2], Khadija M. Alawi[1,2], Julia Rodrigues[1,2], Amit Singh[3], Anjali P. Kusumbe[3], and Saravana K. Ramasamy[1,2,*]

[1]Institute of Clinical Sciences, Imperial College London, London W12 0NN, UK

[2]MRC London Institute of Medical Sciences, Imperial College London, London W12 0NN, UK

[3]The Kennedy Institute of Rheumatology, University of Oxford, Oxford OX3 7FY, UK

[*]Author for correspondence:

Saravana K. Ramasamy
MRC London Institute of Medical Sciences
Imperial College London
Du Cane Road
London W12 0NN, UK
s.ramasamy@imperial.ac.uk
Phone: +44 20 838 31182; Fax: +44 20 838 38303

Key words: Growth plate, osteoclasts, cartilage resorption, endothelial cells, bone shape

**ABSTRACT**

Growth plate cartilage contributes to the generation of a large variety in shapes and sizes of skeletal elements in the mammalian system. The removal of cartilage and how this process regulates bone shape are not well understood. Here we identify a non-bone-resorbing osteoclast subtype termed vessel associated osteoclast (VAO). Endothelial cells (ECs) at the bone-cartilage interface support VAOs through a RANKL-RANK signaling mechanism. Contrary to classical bone associated osteoclasts (BAOs), VAOs are dispensable for cartilage resorption and regulate anastomoses of type-H vessels. Remarkably, proteinases including Matrix metalloproteinase-9 (Mmp9) released from ECs, not osteoclasts, are essential for resorbing cartilage to lead directional bone growth. Importantly, disrupting the orientation of angiogenic blood vessels by misdirecting them results in contorted bone shape. This study identifies proteolytic functions of ECs in cartilage and provides a framework to explore tissue lytic features of blood vessels in fracture healing, arthritis and cancer.

## INTRODUCTION

Endochondral ossification is a fundamental bone forming process involved in skeletal development[1, 2], fracture repair[3, 4] and formation of haematopoietic stem cell niches[5, 6]. This process involving the gradual replacement of cartilage by bone requires a coordination of both local and systemic signals that control proliferation, apoptosis, differentiation and migration of cells[1]. This is all the more remarkable considering the complex coordination of multiple cell types and factors that organise replacement of cartilage with bone to achieve typical shapes that fit with their physiological functions.

Osteoclasts, matrix digesting cells of the skeletal system were proposed to remove cartilage to make lacunae for blood vessels growth[7]. They are suggested to be a heterogeneous population involved in resorbing diverse skeletal surfaces such as bone, cartilage and dentine[8, 9]. However, the existence of cartilage resorbing osteoclasts, sometimes termed chondroclasts has been debatable for a long time because of the lack of *in vivo* or *in situ* characterisation.

The elongation of endochondral bones occurs at the growth plate cartilage[1, 10] where proliferating and differentiating chondrocytes release Vascular Endothelial Growth Factor (VEGF) to attract blood vessels[11]. Blood vessel growth is associated with bone formation during endochondral ossification[12, 13]. A specialised blood vessel subtype, termed type-H, expressing high levels of endothelial markers CD31 and endomucin couples angiogenesis and osteogenesis[14, 15]. Age associated decline in bone mass is associated with the loss of this specialised blood vessel capillaries[14, 16].

In this study, we identify a distinct subset of osteoclasts to be closely associated with type-H capillaries and is found to not spread over skeletal surfaces. Specific association with type-H capillaries makes these osteoclasts to populate bone during formation than resorption. We further demonstrate functions of these osteoclasts and blood vessels in removing cartilage

matrix that has implications for improving healing of bone fractures and provides insight into the way pathologies such as arthritis and cancer degrade the skeletal matrix.

## RESULTS

### Distinct osteoclast subtypes in bone

In order to understand cartilage replacement at the growth plate, we first characterised osteoclast subtypes involved in cartilage resorption. We performed high-resolution three-dimensional confocal immunofluorescence imaging with several *in vitro* defined osteoclast markers along with tartrate resistant alkaline phosphatase (TRAP) to gain detailed insight into the distribution of osteoclasts in bone. TRAP and Integrin-beta-3 (Itgb3) expressing osteoclasts were predominantly localised in the metaphysis (Fig. 1a,b; Supplementary Fig. 1a,b). Another osteoclast marker, V-type proton pump-3 (Vpp3) expression specifically identified osteoclasts and was undetectable in circulating cells in the bone marrow cavity (Fig. 1c; Supplementary Fig. 1c). The distribution of Vpp3+ osteoclasts in the metaphysis was similar to TRAP+ or Itgb3+ osteoclasts. We also visualised osteoclasts using inducible *Csf1r*$^{Mer\text{-}iCre\text{-}Mer}$ (Ref. 17) *Rosa26-tdTomato*[18] double transgenic mice (Supplementary Fig. 1d). Both the strategies uncovered distinct localisation of osteoclasts in bone. In the metaphysis, osteoclasts were preferentially localised at the bone-cartilage interface (proximal) and on the trabecular bone surface (distal).

Comparing phenotypes of these osteoclasts demonstrated that distal osteoclasts were large (60-100um), multinucleated (~4-6) cells displaying characteristics of previously defined bone resorbing osteoclasts, in comparison to relatively smaller (15-20um), 1-2 nucleated proximal osteoclasts (Fig. 1d). Apart from osteoclast markers expression (Fig. 1a-c; Supplementary Fig. 1e), cell size and shape of these cells suggested that proximal osteoclasts were not circulating macrophages/monocytes.

Cathepsin K (Ctsk) expression could demarcate these osteoclast subtypes, as proximal osteoclasts were $Ctsk^{low}$ population compared to high expressing distal osteoclasts (Supplementary Fig. 1e). Interestingly, proximal osteoclasts were closely associated with type-H vessels, which play important role in developmental and regenerative osteogenesis[14-16] rather than skeletal surfaces. Specifically, they interacted with bulge and arch structures[16] of type-H capillaries (Fig. 1e,f) while distal osteoclasts were stretched along bone surfaces. They did not express pro-angiogenic macrophage markers[19] such as Tie2 and Nrp1 (Supplementary Fig. 1f,g). Distal osteoclasts (~60%) on bone surfaces outnumbered vessel associated proximal osteoclasts (~40%) in 4-week old mouse tibia (Supplementary Fig. 1h). Based on these findings, we propose the following terminology: vessel associated osteoclasts (VAO) for the proximal osteoclasts and bone associated osteoclasts (BAO) for the distal osteoclasts in the metaphysis (Fig. 1g).

**Characterisation of osteoclast subsets**

Macrophages migrate from foetal liver to various tissues and organs during early development to form tissue-specific resident macrophages[20]. The origin of VAOs and BAOs were investigated by genetically pulse-chasing foetal liver macrophages using *Csf1r*$^{Mer\text{-}iCre\text{-}Mer}$, *Rosa26-tdTomato* double transgenic mice. After a single tamoxifen injection at embryonic day 12.5 (E12.5), bones were analysed on E17.5, P3, P14 and P28. Pulse-chasing foetal liver macrophages showed that both osteoclast subtypes were derived from foetal liver macrophages (Fig. 2a). Similarly, we performed fate-mapping in early postnatal bones by pulse-labelling of cells at P10. This labelled a few macrophages when observed at 6 and 12hpi (hours post injection) but both VAOs and BAOs were not labelled. Despite weak labelling at 24hpi, both osteoclast subtypes were labelled on 24, 48 and 120hpi (Supplementary Fig. 1i). To understand the relationship further, we labelled phagocytic cells

by injecting liposome encapsulated DiI dye (LED). In 6hpi bones, LED was detected primarily in diaphyseal macrophages and a very few cells in the metaphysis. Labelling of both VAOs and BAOs at 24hpi in the metaphysis established the concurrent generation of both the osteoclast subsets from macrophages (Supplementary Fig. 1j). 5-ethynyl-2′-deoxyuridine (EdU) labelling revealed non-proliferative nature of the osteoclast subtypes (Fig. 2b). Remarkably, transplantation of VAO subsets into sub-lethally irradiated mice resulted in formation of both VAOs and BAOs indicating the potential of VAO subset to form BAOs (Fig. 2c). BAOs did not survive transplantation assay.

To gain insight into their molecular properties, RANK+ total osteoclasts in bone were sorted by flow-cytometry into VAOs (2 nuclei) and BAOs (>4 nuclei) based on the nuclei number (Fig. 2d,e; Supplementary Fig. 1k). The purified osteoclast subsets were subjected to RNA-sequencing (RNAseq) analysis. Both subtypes displayed distinct expression profiles suggesting the independent nature of these osteoclasts. Differential gene expression analysis identified 950 genes with False Discovery Rate (FDR)-adjusted P-value<0.05 (Fig. 2f; Supplementary Table 1). Similar to immunostaining results, *Ctsk* transcript levels were reduced in VAOs compared to BAOs (Fig. 2g). We further subjected freshly purified osteoclasts to quantitative PCR with reverse transcription for a panel of differentially regulated genes and validated RNAseq results to confirm distinct expression profiles of osteoclast subsets (Fig. 2h).

These observations established spatial and phenotypic heterogeneity in osteoclasts of long bones, which also applied to other skeletal structures in mice such as vertebra and sternum. Absence of VAO subsets in calvarium and compact bone indicated their specificity to endochondral ossification (Supplementary Fig. 2a-d).

**Bone endothelium supports VAO subtype**

Bone remodels continuously and shows remarkable changes with age. We analysed osteoclasts distribution with age-related changes in bone. Randomly distributed osteoclasts in early foetal bones showed selective positioning in postnatal bones with the alignment of type-H and -L capillaries (Fig. 3a). Quantification of total osteoclasts showed remarkable decline in osteoclast population in bones of ageing mice (Fig. 3b) and this decrease correlated with the age-dependent reduction in type-H capillaries[14, 16]. VAOs were predominant in early developing bones while BAOs were the major subtype occupying ageing bones (Supplementary Fig. 2e). Stage specific distribution of osteoclast subtypes indicated the prevalence of VAOs during developmental bone formation and BAOs during age-related bone loss.

The developmental association of VAOs with type-H capillaries and their age-dependent reduction intrigued us to investigate their interaction in regenerative conditions. Exposure to irradiation injury led to a significant increase in VAO number (Fig. 3c) coinciding the increase in type-H vessels[14]. We first reduced type-H numbers pharmacologically using SU5416, an anti-angiogenic drug inhibiting VEGF Receptor-2[21]. Systemic SU5416 treatment led to a decline in VAO subset (Supplementary Fig. 2f-h). We also manipulated type-H ECs genetically by targeting endothelial Notch signaling as described earlier[15]. This involves deletion of Delta-like ligand 4 (Dll4) and F-Box and WD repeat domain containing7 (Fbxw7) in ECs using *Cdh5(PAC)-CreERT2* mice. Tamoxifen inducible *Cdh5(PAC)-CreERT2*[14-16, 22-24] specifically targets ECs in postnatal mouse bones (Supplementary Fig. 2i,j). Genetic reduction of type-H ECs ($Dll4^{i\Delta EC}$) led to a decline in VAO subset (Supplementary Fig. 3a). Conversely, promotion of type-H ECs ($Fbxw7^{i\Delta EC}$) increased VAO number (Supplementary Fig. 3b). Endothelial deletion of Von Hippel-Lindau Tumor Suppressor (Vhl) was earlier demonstrated to promote type-H ECs[14, 23]. We reactivated type-H ECs in aged mice by inducible endothelial specific Vhl deletion ($Vhl^{i\Delta EC}$)

which led to reappearance of VAOs in aged tibia (Supplementary Fig. 3c). This again established the importance of type-H in regulating VAO subset. Remarkably, both *Dll4*$^{i\Delta EC}$ and SU5416 treated bones showed dramatic increase in growth plate size in comparison to respective controls (Fig. 3d,e; Supplementary Fig. 4a,b). We found accumulation of apoptotic cells in these growth plates, and expression of Collagen-X and MMP13 in the hypertrophic zone (Supplementary Fig. 4a-f). This suggested defective replacement of chondrocytes and matrices in these animals.

**Molecular interaction between VAOs and type-H ECs**

To gain molecular insight into the association of VAOs with type-H, we FACS sorted type-H and type-L ECs, and analysed transcripts for important factors with known roles in osteoclast generation. Transcripts of important osteoclastogenic factors such as *Csf1, Il1a* and *Tnfsf11a* were highly expressed in type-H compared to type-L ECs (Fig. 3f). Tnfsf11a (RANKL) serves as a ligand to signal RANK expressing preosteoclasts in mediating osteoclast differentiation and activation[8, 25, 26]. High expression of *Tnfsf11a* in type-H ECs argues for the possible involvement of RANKL-RANK signalling between type-H ECs and VAOs. To investigate this, inducible EC-specific loss-of-function mice were generated using loxP-flanked *Rankl* alleles (*Rankl*$^{lox/lox}$)[27] and *Cdh5(PAC)-CreERT2* transgenics. Following tamoxifen administration from postnatal day(P) P10 to P14, analysis of *Rankl*$^{i\Delta EC}$ mutants at P28 demonstrated reduction of *Tnfsf11* transcripts specifically in ECs (Supplementary Fig. 4g). Endothelial specific loss of Tnfsf11a (*Rankl*$^{i\Delta EC}$) reduced VAO subset in bones along with a decrease in total osteoclasts number (Fig. 3g,h). These mutants showed increase in trabecular bone, while type-H ECs were unaltered (Supplementary Fig. 5a-d). To understand osteoclast phenotype, we injected DiI-labelled liposomes to visualise localisation of new phagocytic cells near mutated vessels. Specific absence of DiI-labelled phagocytes near type-

H vessels but unaffected bone surface suggested unsuitable microenvironment provided by *Rankl*$^{i\Delta EC}$ endothelium (Supplementary Fig. 5e). This established the importance of Rankl in type-H ECs to regulate VAO number. Remarkably, growth plates of *Rankl*$^{i\Delta EC}$ mutants showed unaltered collagen-X and MMP13 expression, and apoptotic cells in the hypertrophic zone (Fig. 3i; Supplementary Fig. 5f).

**VAOs are dispensable for the growth plate resorption**

Reduced osteoclasts with unaltered growth plates in *Rankl*$^{i\Delta EC}$ mutants prompted us to investigate the cartilage resorptive function of osteoclasts by depleting osteoclasts genetically and pharmacologically. Bisphosphonates, a class of anti-resorptive drugs, functions majorly by inhibiting osteoclasts[28, 29]. Administration of alendronate (1mg/kg weight of mouse) twice-a-week for 4 weeks led to increased bone mass and reduced osteoclasts number without affecting growth plate size (Fig. 4a,b; Supplementary Fig. 6a,b). The expression of the matrix protein, collagen-X and apoptotic cells in the hypertrophic zone of alendronate treated mice were similar to control animals (Fig. 4c; Supplementary Fig. 6c). We also analysed bones of mice showing severe osteopetrotic (*op/op*) mutation which display defective osteoclasts, macrophages and monocytes[30, 31]. Despite having impaired osteoclast functions, growth plates of 21-day-old *op/op* mice remained unaffected (Fig. 4d). Thus, these results indicated that defective osteoclasts function did not affect cartilage resorption in bones.

To understand VAO functions, we targeted VAO subtype specifically by short-term bisphosphonate treatment without altering BAO subset. This VAO depletion could be maintained for 7days with intermittent bisphosphonate administration for 3 days (Fig. 4e; Supplementary Fig. 6d). The elongated type-H capillaries in treated bones showed significant decrease in arch structures in the vascular front (Fig. 4e,f). Arch structures in type-H capillaries are formed by anastomoses of bulges in the leading front[16]. Reduction in arch

structures upon VAO depletion suggested the involvement of VAOs in anastomosis of type-H bulges. Because formation of bulges and arches is apparent in juvenile bones[16], we depleted VAOs in 2-weeks-old mice to investigate formation of these angiogenic structures on blood vessels. We used liposome encapsulated bisphosphonates (LEB) to target osteoclasts and macrophages specifically. Similar to alendronate, short-term administration of LEB caused specific depletion of VAO subset (Fig. 4g). VAO depletion resulted in disturbed symmetry at the bone-cartilage interface. Absence of anastomoses led to unequal invasion of blood vessels with some individual blood vessels elongate more into growth plate cartilage while some lag behind (Fig. 4h), resulting in formation of disturbed epiphysis line. Thus, VAOs play role in maintaining the boundary of bone-cartilage interface by mediating anastomoses of bulge structures in the vascular front. Number of bulges and their anastomoses decrease with age[16] which supports the unaltered epiphysis line observed in long-term alendronate treated bones.

**Type-H endothelium can digest cartilage matrix**

The dispensable function of VAOs in cartilage resorption indicated the potential involvement of type-H ECs in the phenotypes observed earlier (Fig. 3d,e; Supplementary Fig. 4). Type-H ECs being the leading structures in the epiphyseal bone growth (see blood vessels and VAO localisations in all control figures) corroborates the significance of these cells in resorbing cartilage matrix. Analysing osteoclast localisation in the primary ossification centre of foetal long bones (Fig. 5a) confirmed ECs as the leading structures during endochondral ossification. To understand the involvement of type-H ECs in resorbing cartilage matrix, pure type-H ECs, BAOs, VAOs were sorted by flow cytometry from femurs to perform gene expression analysis of proteinases with known roles in skeletal matrix digestion. Transcripts of proteinases such as *Bmp1, Timp1, Timp2, Timp3, Timp4, Mmp2, Mmp9, Mmp14, Adamts1*

and *Adamts5* were significantly higher expressed in type-H ECs relative to both the osteoclast subtypes (Fig. 5b).

Type-H ECs displayed highest fold expression (40-fold) for *Mmp9* transcripts in comparison to VAOs and BAOs. Global deletion of Mmp9 gene resulted in defective growth plate with large hypertrophic zone[32], reminiscent of blood vessel mediated defects. To analyse endothelial specific function of these proteinases in resorbing cartilage matrix, we generated conditional *Mmp9* transgenic mouse line to induce deletion in ECs or osteoclasts using *Cdh5(PAC)-CreERT2* and *Csf1r*$^{Mer\text{-}iCre\text{-}Mer}$ drivers respectively. Following tamoxifen administration from P10 to P14, these transgenic animals were analysed on P28 to investigate resorption of growth plate cartilage. Targeting of *Mmp9* in postnatal endothelium in bone (*Mmp9*$^{i\Delta EC}$) led to the formation of large growth plates (Fig. 5c,d; Supplementary Fig. 6e). These growth plates showed increase in number of apoptotic cells and both Collagen-X and MMP13 expression (Fig. 5c; Supplementary Fig. 6f,g) in the hypertrophic zone of mutants compared to littermate controls. No obvious change in blood vessel phenotype was observed in these mutants (Fig. 5e). Conversely, inducible targeting of *Mmp9* in postnatal osteoclasts (*Mmp9*$^{i\Delta OC}$) did not lead to appreciable changes in osteoclasts number or in growth plate size compared to their littermate controls (Fig. 5f-h; Supplementary Fig. 6g,h). Thus, the above findings support the crucial role of EC-derived Mmp9, in invading cartilage matrix during bone formation.

**Type-H mediated cartilage replacement mediates the directional elongation of bone**

The elongation of an endochondral bone occurs at the growth plate. The growth rate and differential elongation rates of various skeletal elements are majorly structured by the longitudinal expansion of hypertrophic chondrocytes in the direction of growth within constraining matrix canals[1, 10, 33-37]. Remarkably, leading structures of type-H capillaries were

directed towards hypertrophic chondrocytes and seemed aligned with the matrix canals (Fig. 6a). Quantification of angular orientations of blood vessels in bone sections established that type-H capillaries were polarised towards chondrocytes and positioned along the axis of bone elongation. This directional growth of type-H vessels towards the direction of bone elongation was observed not only in linear growth, but also in three-dimensional growth observed at secondary ossification centres (Fig. 6b-e; Supplementary Fig. 6i). These observations also correlated with the direction of elongation seen in other endochondral skeletal elements (Supplementary Fig. 2a-d, 7a). The cartilage resorbing function and directional orientation of type-H ECs intrigued us to question whether ECs provide directional cues during bone elongation. To investigate this, we redirected type-H vessels to test whether elongation of long bone occurs at a different orientation. We combined *Dll4*$^{i\Delta EC}$ mice with alendronate treatment to generate growth of misdirected blood vessels and investigated directional bone growth in postnatal tibia. Endothelial Dll4 mutant bones show formation of defective and irregular blood vessels during postnatal development[15]. Alendronate treatment promotes blood vessel growth[16] and simultaneously inhibits osteoclasts, a prerequisite condition required to investigate EC-specific functions in bone remodelling. Tamoxifen was administered from P35 to P39 to induce recombination, followed by alendronate treatments from P40 for 4 weeks on every alternate day (Fig. 7a). Targeting Dll4 in postnatal endothelium (*Dll4*$^{i\Delta EC}$) resulted in irregularly arranged type-H vessels and increased growth plate size at P70. Combining alendronate administration promoted growth of randomly directed blood vessels and led to the uneven invasion of the growth plate by blood vessels (Fig. 7b). This in turn resulted in disproportionate removal of cartilage matrix in the growth plate leading to changes in bone shape. Remarkably, no proper growth plate was observed in these animals (Fig. 7c-e). Epiphyseal regions of these bones displayed cartilage islands, which potentially appeared as a result of surrounding blood

vessels (Supplementary Fig. 7b). Thus, irregular invasion of the growth plate by blood vessels led to misdirected elongation of bone, displaying abnormal orientation (shape). However, presence of osteoclasts particularly VAO subsets would promote anastomoses of newly formed blood vessels and inhibit this irregular invasion of cartilage. To test this, we promoted new blood vessel growth in *Dll4*$^{i\Delta EC}$ mice without inhibiting osteoclasts by intermittent parathyroid hormone (PTH; 100µg/kg wt mice) administration. Intermittent PTH increases bone blood flow[38, 39] and was shown to not affect osteoclast activity[40]. Remarkably, PTH mediated growth of new blood vessels in *Dll4*$^{i\Delta EC}$ mice displayed limited elongation into the cartilage matrix. Formation of new type-H vessels in these animals was associated with revival of VAO subset which in turn promoted anastomoses of type-H capillaries. This resulted in limited invasion of cartilage and no change in bone orientation was observed (Supplementary Fig. 7c-f). In addition to estbalishing the role of blood vessels in directing bone elongation, this finding also suggested the supportive role played by VAOs in assisting the blood vessel growth.

## DISCUSSION

The cellular and molecular mechanisms involved in directing the individual bones to acquire their characteristic shapes during endochondral ossification are poorly understood. The elongation of endochondral bones at the growth plate involves continuous replacement of cartilage matrix by calcified bone to achieve their typical shapes. In addition to developmental bone formation, cartilage resorption is an important mechanism during repair process after fracture or injury[3, 41, 42]. Pathological conditions like arthritis[43, 44] and cancer involve unregulated removal of cartilage matrix and bone formation[45-48]. The cellular composition, organisation and regulation of bone-cartilage interface mediating replacement

of cartilage and directional elongation of skeletal elements are long standing fundamental questions in the skeletal physiology.

In this study, we identified and classified osteoclast subtypes based on their structures and localisation- VAOs and BAOs. While BAOs are classical osteoclasts, VAOs regulate blood vessel growth in bone. RNA sequencing data demonstrated distinct expression profiles of VAOs and BAOs. Additionally, characterisation of VAOs also established that VAO subsets are different from previously recognised pre-osteoclast and macrophage populations[49, 50]. The prevalence of VAO during bone formation and BAO in bone loss provides a fundamental approach to consider both the subtypes in order to understand the resorption status of bone. Investigating osteoclasts subtypes in developmental bone diseases will provide additional perspectives to understand the pathological conditions better and develop effective therapeutic strategies.

Despite blood vessels being identified as an important component of endochondral bone growth, their role in the removal of cartilage matrix has not been recognised. Inhibiting blood vessel growth results in enlarged growth plate size due to the defective cartilage resorption. This matrix digesting function of endothelium is supported by the enlarged growth plate phenotype observed in a number of studies that affected angiogenic growth of blood vessels in bone[11, 15, 51]. This finding is particularly important to understand pathology of conditions associated with tissue degeneration and damage as observed in osteoarthritis, ageing, fracture-repair and cancer. Together, our findings illustrate previously unknown function of ECs in skeletal matrix resorption, which provides the framework for understanding differential elongation of various skeletal elements and for investigating skeletal pathologies.

**Ethical review**

All animal experiments were performed in compliance with the relevant laws and

institutional guidelines and were approved by local animal ethics committees.

**Acknowledgements**. We thank A. Duarte, F. Radtke and A. Behrens for floxed *Dll4* and *Fbxw7* mutant mice. We thank Laurence Game and Ivan Andrew from LMS Genomics facility. We thank Gopuraja Dharmalingam from LMS Bioinformatics for helping with R analysis. We also thank LMS/NIHR flow facility and CBS at the Imperial College London for technical support. We thank Pengjun Xi for mice injections. S.K.R is a Sir Henry Dale Fellow of the Wellcome Trust and the Royal Society (202300/Z/16/Z). Funding to S.K.R was provided by the Wellcome Trust, the Royal Society, the Medical Research Council and the American Bone and Mineral Research Society. A.P.K is supported by the Medical Research Council (CDA- MR/P02209X/1), the Kennedy Trust for Rheumatology Research (AZR00700) and Leuka.

**Author Contributions.** S.G.R. and K.M.A designed and performed most of the experiments and interpreted results. J.R. performed immunostainings and generated confocal images. A.S. generated RNA sequence data. A.P.K provided tools, designed experiments and interpreted results. All the authors prepared the manuscript. S.K.R. conceived the study, designed and performed experiments, interpreted results and wrote the manuscript.

**Declaration of interest**

The authors do not declare competing financial interests.

## Figure legends

### Fig. 1: Osteoclast subtypes in bone

**a,** Tile scan image shows distribution of Itgb3+ (green) cells in 3-week-old tibia across 5 independent experiments. Endomucin (Emcn, red) shows arrangement of blood vessels. Insets show localisation of Itgb3+ cells in relation to blood vessels in the metaphysis (mp, blue box) and in the diaphysis (dp, yellow box). growth plate, gp; compact bone, cb. Scale bars, 500μm; insets, 50μm(top), 70μm (bottom).

**b,** Maximum intensity projection of TRAP (green) expressing cells along with Endomucin stained blood vessels (Emcn, red) in the tibial metaphysis of a 3-week old mouse from 3 independent experiments. Scale bar, 50μm.

**c,** Confocal images showing distribution of osteoclasts and blood vessels in the tibial metaphysis of a 3-week old mouse from 4 independent experiments. Vpp3 (green) and Endomucin (Emcn, red) stained to identify osteoclasts and blood vessels respectively. Blue arrow indicates proximal osteoclasts and white arrow indicates distal osteoclasts. Scale bar, 50μm.

**d,** Representative images show proximal and distal osteoclasts immunostained with Vpp3 (green). Endomucin (Emcn, red) marks blood vessels and DAPI is a nuclear counterstain. Scale bars, 20μm. Quantification of size and number of nuclei present in osteoclast subtypes localised in the proximal and distal region of the tibial metaphysis. Data represent mean ± sem. *P* values, two-tailed unpaired *t*-tests. Data points were pooled across multiple bone samples n=27 and n=28 for osteoclasts size and nuclei quantifications respectively.

**e,** Confocal images showing localisation of proximal and distal osteoclasts (Vpp3, green) in the metaphysis with respect to blood vessels (Emcn, red) from 4 independent experiments. Proximal osteoclasts are largely in close contact with blood vessels (blue arrow) while majority of distal osteoclasts are not (white arrow). Inset is an optical section of the image

showing close association of blood vessels and osteoclasts in all three planes. Nuclei, DAPI. Scale bars, 20μm.

**f,** Transverse section of tibial metaphysis shows localisation of blood vessels (Emcn, red) and osteoclasts (Vpp3, green) from 3 independent experiments. Nuclei, DAPI. Scale bar, 50μm.

**g,** Schematic representation of osteoclasts distribution in the bone metaphysis.

**Fig. 2: Characterising osteoclasts subtypes in bone**

**a,** Lineage tracing foetal liver macrophages using *Csf1r* $^{Mer\text{-}iCre\text{-}Mer}$ and *R26-tdTomato* mice. Tamoxifen was injected at E12.5 and tdTomato expression was traced at E17.5, P3, P14 and P28 in 3 independent experiments. Vessels (CD31, red), Osteoclasts (Itgb3, green), Nucleus (DAPI, blue). Scale bars, 50μm (E17.5, P14, P28), 100μm (P3).

**b,** 5-ethynyl-2′-deoxyuridine (EdU) labelling (magenta) in P14 mouse tibia from 3 independent experiments showed both osteoclasts subtypes (Itgb3, green) were not proliferating. DAPI (blue) stains nucleus. Scale bar, 50μm.

**c,** Sorted tomato+ VAO subset was transplanted into irradiated recipients. Transplanted VAOs occupied bone surface in addition to blood vessels in 3 independent experiments. Scale bars, 50μm

**d,** Representative flow cytometry plots show sorting profile used to separate VAOs and BAOs in 10 independent experiments. RANK+ cells with 2 nuclei (VAO) and >4 nuclei (BAO) are sorted for gene expression analysis.

**e,** RANK and Vybrant stained cells were imaged after sorting in 3 independent experiments to ensure purity. Scale bars, 20μm.

**f,** Heat map shows RNASeq expression levels of differentially expressed (DE) genes between VAO and BAO (FDR-adjusted *P* value cutoff < 0.05 with coding biotype). The color code

indicates the normalized log2-transformed counts per million reads with upregulated (red) and downregulated (blue) genes. Volcano plot shows DE genes comparing BAO with VAO. DE genes were calculated using negative binomial Wald function and p-values were adjusted using Benjamin-Hochberg method. Cells sorted from 5 independent experiments were pooled into 2 samples for RNAseq.

**g,** Cathepsin K transcripts (*Ctsk*) in RNA sequenced samples of VAO and BAO subsets using n=2 samples pooled from 5 independent experiments. RPKM, reads per kilobase per million mapped reads. Data represent mean values.

**h,** Purified VAO and BAO subset were subjected to quantitative PCR analysis for validating selected genes to confirm their expression pattern across independent experiments. Data represent mean ±sd. *P* values, two-tailed unpaired *t*-tests, Welch's correction performed in sets with unequal sample numbers, n numbers represent biological replicates, pooled from 8 experiments, and are indicated as data points in the graph. Source data are available in Supplementary Table 2.

**Fig. 3: Association of blood vessels and osteoclasts**

**a,** Images show age-dependent distribution of osteoclasts using Itgb3 (green, osteoclasts) and Emcn (red, vasculature) immunostaining. DAPI, Nuclei. White arrows in 10- and 80-weeks indicate BAOs. Scale bars, 150µm (E17.5), 50µm (P0,P70,P560), 100um (P7,P14). Representative image of 4 independent experiments.

**b,** Quantification of total osteoclasts shows age dependent decline in number across n=5 biological replicates pooled from 3 experiments. Data represent mean ± sem.

**c,** Representative images show distribution of osteoclasts in 8-week-old control and irradiated mice tibia from 4 independent experiments. Emcn (red, vasculature), Itgb3 (green, osteoclasts). Scale bars, 50µm. Quantification of VAOs shows increase in VAO number in

n=6 irradiated bones pooled from 4 experiments. Data represent mean ± sem. *P*-values, two-tailed unpaired *t*-tests.

**d,** Confocal image showing growth plates of vehicle (control) and Vegfr2 inhibitor (SU5416) injected tibia of 4-week-old mice. Emcn (red, vasculature), DAPI (blue, nucleus). Scale bars, 200µm. Representative image from 4 independent experiments.

**e,** Graph shows increased growth plate size of tibia in Vegfr2 inhibitor (SU5416) treated mice from n=6 animals pooled from 4 experiments. Data represent mean ±sem. *P*-values, two-tailed unpaired *t*-tests.

**f,** qPCR analysis of pro-osteoclastogenic factors expressed on sorted bone ECs– type-H and type-L. Relative fold expression in type-H ECs calculated compared to type-L. Transcripts expression for each gene were normalised to beta-actin levels. Data represent mean ± sd. *P*-values, two-tailed unpaired *t*-tests, n numbers represent biological replicates, pooled from 4 experiments, and are indicated as data points in the graph. Source data are available in Supplementary Table 2.

**g,** Representative images of blood vessels (Emcn, red) and osteoclasts (Vpp3, green) in the metaphysis of *Rankl* $^{i\Delta EC}$ mutants and their 4-week-old littermate controls. Scale bars, 50µm. Representative image from 4 independent experiments.

**h,** Quantification of both the osteoclasts subtypes in tibia of *Rankl* $^{i\Delta EC}$ mutants across n=12 bone samples pooled from 4 independent experiments. Data represent mean ±sd. *P*-values, two way-ANOVA with Sidak's multiple comparisons test.

**i,** Graph shows measurement of growth plate sizes in *Rankl* $^{i\Delta EC}$ mutants and their littermate controls from n=6 animals. Data represent mean ±sd. *P*-values, two-tailed unpaired *t*-tests.

**Fig. 4: Role of osteoclasts in regulating growth plate size**

**a,** Confocal images show distribution of osteoclasts (Itgb3, green) in alendronate and control treated tibia of 4-week-old mice. Emcn, vasculature (red); DAPI, nuclei (blue). Scale bars, 50μm. Representative image from 3 independent experiments.

**b,** Graph shows measurement of growth plate sizes in control and alendronate treated mice from n=6 biologically independent animals. Data represent mean ± sem. *P* values, two-tailed unpaired *t*-tests.

**c,** Graph shows quantification of TUNEL+ cells in hypertrophic zones of growth plates from n=6 biologically independent animals. Data represent mean ± sem. *P* values, two-tailed unpaired *t*-tests.

**d,** Confocal images show growth plate in 3-week-old control and *op/op* mice from 3 independent litters. Emcn, vasculature (red); DAPI, nuclei (blue). Scale bars, 200μm. Quantification of growth plate sizes from n=5 control and n=6 *op/op* animals confirm unaltered size in osteopetrotic mutants. Data represent mean ± sem. *P* values, two-tailed unpaired *t*-tests with Welch's correction.

**e,** Short-term alendronate treatment shows specific depletion of VAO subset of osteoclasts. Images show osteoclasts (Itgb3, green) and blood vessel (Emcn, red) arrangements in control and alendronate treated 3-week-old mice. White arrows in alendronate treated bone sections indicate a few single (not anastomosing) bulge structures. Scale bars, 50μm. Representative image from 3 independent experiments.

**f,** Graph shows quantification of anastomosing bulge structures in the vascular front of control and alendronate treated bones from n=9 biologically independent animals. Data represent mean ± sem. *P* values, two-tailed unpaired *t*-tests.

**g,** Representative image shows osteoclast (Itgb3, green) distribution at the metaphysis metaphysis of 4-week-old short-term control and liposome encapsulated clodronate administered mice from 3 independent experiments. Scale bars, 50μm.

**h,** Tile scan images show the growth plate in control and liposome encapsulated clodronate treated 4-week-old mice from 3 independent experiments. Insets show blood vessel (Emcn, red) and osteoclasts (Itgb3, green) staining at the disturbed epiphysis region compared to controls. White arrows indicate a few uneven blood vessel invasions in the vascular front. Scale bars, 200µm; insets, 50µm.

**Fig. 5: Role of blood vessels in cartilage resorption**

**a,** Images show capillaries (Emcn, red) and osteoclasts (Itgb3, green) localisation during primary ossification in mouse limbs. pc, perichondrium. Scale bars, 50µm(E12.5), 30µm(E13.5, E14.5). Representative image from 4 independent experiments and several repeated observations.

**b,** Quantitative PCR comparing transcript levels of bone proteinases in purified type-H ECs, BAOs and VAOs. Relative fold expression is calculated in type-H ECs and VAOs, compared to BAOs. Gene expression is normalised to beta-actin levels. Data represent mean ± sem. *P* values, one-way ANOVA with Tukey's multiple comparison test, n numbers represent biological replicates, pooled from 4 experiments, and are indicated as data points in the graph. Source data are available in Supplementary Table 2.

**c,** Tile scan images of *Mmp9* $^{i\Delta EC}$ mutants and their 4-week-old littermate controls show Collagen-X (ColX, green) immunostaining in hypertrophic zone. DAPI (blue) is nucleus. Scale bars, 300µm. Representative image from 3 independent experiments.

**d,** Graph shows growth plate measurements in *Mmp9* $^{i\Delta EC}$ mutants and littermate controls from n=6 biologically independent animals. Data represent mean ± sem. *P* values, two-tailed unpaired *t*-tests.

**e,** Confocal image shows blood vessels arrangement (CD31, green) and osteoclast (Vpp3, magenta) distribution in *Mmp9* $^{i\Delta EC}$ mutants and littermate controls from 4 independent experiments. Scale bars, 50µm

**f,** Maximum intensity projection of tibial metaphysis in *Mmp9* $^{i\Delta OC}$ mutants and their 4-week-old littermate controls from 4 independent experiments. Images show distribution of osteoclasts are not affected in these osteoclast specific mutants. Emcn, blood vessels (red); Itgb3, osteoclasts (green); DAPI, nuclei (blue). Scale bars, 50µm

**g,** Tile scan confocal image illustrates the unaffected growth plate size in *Mmp9* $^{i\Delta OC}$ mutants in comparison to their control littermates. Blood vessels were immunostained with Endomucin (red). DAPI is nuclei counterstain. Scale bars, 200µm. Representative image from 3 independent experiments.

**h,** Quantification graph of growth plate sizes in *Mmp9* $^{i\Delta OC}$ mutants and their littermate controls from n=6 independent animals. Data represent mean ± sem. *P* values, two-tailed unpaired *t*-tests.

**Fig. 6: Type-H capillaries guide bone growth direction**

**a,** Confocal image shows invading blood vessels in the growth plate. CD31 (green) immunostained bulge structures of type-H capillaries can be seen aligned with the chondrocyte matrix channels (DIC) from 6 repeated experiments. White arrows indicate the direction of blood vessel growth. Scale bar, 10µm

**b,** Tile scan images of developing mouse tibia were immunostained for Endomucin (red), CD31 (green) show the presence of type-H vessels in the leading direction of blood vessels growth as observed from 12 independent experiments. White arrows indicate the direction of blood vessel growth. The orientation is always towards the direction of bone elongation. DAPI is nuclear counterstain. Scale bars, 200µm (E15.5,P0), 500µm(P7, P28).

**c,** Angle histogram plots show directional distribution of type-H, type-L capillaries and chondrocytes relative to the direction of bone elongation. Orientations of type-H and chondrocytes were calculated on proximal end of tibia. Type-L capillaries orientations were measured from diaphysis.

**d,** Transverse sections of mouse tibial proximal head at various stages of development illustrate the orientation of type-H vessels and the direction of bone enlargement during growth of 6 independent experiments. Endomucin, red; CD31, green; DAPI, blue. Both CD31 and Emcn were immunostained to identify type-H vessels. White arrows indicate the direction of blood vessel growth. DAPI is nuclear counterstain. Scale bars, 250μm (P10,P28), 300μm(P14, P21).

**e,** Graphical illustration to show the relation between the directional growth of type-H capillaries and bone elongation - linear growth observed during lengthening of long bones and three-dimensional bone enlargements in secondary ossification centres.

**Fig. 7: Role of misdirected blood vessels on bone shape**

**a,** Experimental scheme illustrating the tamoxifen administration and alendronate treatment in *Dll4* transgenic animals for misdirecting blood vessels to investigate their function in directional bone growth.

**b,** Schematic illustration highlighting the behaviour of type-H capillaries in each treatment conditions that first misdirect and then promote blood vessel growth

**c,** Confocal tile scan images show blood vessel (Endomucin, Emcn, red) orientation in 10-weeks old *Dll4* $^{i\Delta EC}$ mutants and littermate control mice treated with alendronate of 3 independent experiments. DAPI stains nuclei. Note growth plate (gp) size and orientation of bone in the treated conditions. Arrows in alendronate treated *Dll4* $^{i\Delta EC}$ mutants indicate cartilage islands. Scale bars, 300μm.

**d,** Maximum intensity projections of mouse tibial metaphysis immunostained for Endomucin (red) to label blood capillaries. *Dll4* $^{i\Delta EC}$ mutants show randomly oriented blood vessels in the metaphysis in comparison to their control littermates of 3 independent experiments. Alendronate treatment promoted growth of this randomly oriented blood vessels leading to irregular resorption of growth plate cartilage. DAPI is nuclear counterstain. Scale bars, 50μm. **e,** Angle histogram plots show directional distribution of type-H capillaries and chondrocytes relative to the proximal distal axis of tibia in *Dll4* $^{i\Delta EC}$ mutants and littermate controls with alendronate administration.

## References


1. Kronenberg, H.M. Developmental regulation of the growth plate. *Nature* **423**, 332-336 (2003).
2. Mackie, E.J., Ahmed, Y.A., Tatarczuch, L., Chen, K.S. & Mirams, M. Endochondral ossification: how cartilage is converted into bone in the developing skeleton. *Int J Biochem Cell Biol* **40**, 46-62 (2008).
3. Bolander, M.E. Regulation of fracture repair by growth factors. *Proc Soc Exp Biol Med* **200**, 165-170 (1992).
4. Einhorn, T.A. The cell and molecular biology of fracture healing. *Clin Orthop Relat Res*, S7-21 (1998).
5. Chan, C.K. *et al.* Endochondral ossification is required for haematopoietic stem-cell niche formation. *Nature* **457**, 490-494 (2009).
6. Reddi, A.H. & Anderson, W.A. Collagenous bone matrix-induced endochondral ossification hemopoiesis. *J Cell Biol* **69**, 557-572 (1976).
7. Lewinson, D. & Silbermann, M. Chondroclasts and endothelial cells collaborate in the process of cartilage resorption. *Anat Rec* **233**, 504-514 (1992).
8. Boyle, W.J., Simonet, W.S. & Lacey, D.L. Osteoclast differentiation and activation. *Nature* **423**, 337-342 (2003).
9. Henriksen, K., Bollerslev, J., Everts, V. & Karsdal, M.A. Osteoclast activity and subtypes as a function of physiology and pathology--implications for future treatments of osteoporosis. *Endocr Rev* **32**, 31-63 (2011).
10. Hunziker, E.B. & Schenk, R.K. Physiological mechanisms adopted by chondrocytes in regulating longitudinal bone growth in rats. *J Physiol* **414**, 55-71 (1989).
11. Gerber, H.P. *et al.* VEGF couples hypertrophic cartilage remodeling, ossification and angiogenesis during endochondral bone formation. *Nat Med* **5**, 623-628 (1999).
12. Kanczler, J.M. & Oreffo, R.O. Osteogenesis and angiogenesis: the potential for engineering bone. *Eur Cell Mater* **15**, 100-114 (2008).

13. Schipani, E., Maes, C., Carmeliet, G. & Semenza, G.L. Regulation of osteogenesis-angiogenesis coupling by HIFs and VEGF. *J Bone Miner Res* **24**, 1347-1353 (2009).
14. Kusumbe, A.P., Ramasamy, S.K. & Adams, R.H. Coupling of angiogenesis and osteogenesis by a specific vessel subtype in bone. *Nature* **507**, 323-328 (2014).
15. Ramasamy, S.K., Kusumbe, A.P., Wang, L. & Adams, R.H. Endothelial Notch activity promotes angiogenesis and osteogenesis in bone. *Nature* **507**, 376-380 (2014).
16. Ramasamy, S.K. *et al.* Blood flow controls bone vascular function and osteogenesis. *Nat Commun* **7**, 13601 (2016).
17. Qian, B.Z. *et al.* CCL2 recruits inflammatory monocytes to facilitate breast-tumour metastasis. *Nature* **475**, 222-225 (2011).
18. Madisen, L. *et al.* A robust and high-throughput Cre reporting and characterization system for the whole mouse brain. *Nat Neurosci* **13**, 133-140 (2010).
19. Fantin, A. *et al.* Tissue macrophages act as cellular chaperones for vascular anastomosis downstream of VEGF-mediated endothelial tip cell induction. *Blood* **116**, 829-840 (2010).
20. Davies, L.C., Jenkins, S.J., Allen, J.E. & Taylor, P.R. Tissue-resident macrophages. *Nat Immunol* **14**, 986-995 (2013).
21. Fong, T.A. *et al.* SU5416 is a potent and selective inhibitor of the vascular endothelial growth factor receptor (Flk-1/KDR) that inhibits tyrosine kinase catalysis, tumor vascularization, and growth of multiple tumor types. *Cancer Res* **59**, 99-106 (1999).
22. Itkin, T. *et al.* Distinct bone marrow blood vessels differentially regulate haematopoiesis. *Nature* **532**, 323-328 (2016).
23. Kusumbe, A.P. *et al.* Age-dependent modulation of vascular niches for haematopoietic stem cells. *Nature* **532**, 380-384 (2016).
24. Wang, Y. *et al.* Ephrin-B2 controls VEGF-induced angiogenesis and lymphangiogenesis. *Nature* **465**, 483-486 (2010).
25. Lacey, D.L. *et al.* Osteoprotegerin ligand is a cytokine that regulates osteoclast differentiation and activation. *Cell* **93**, 165-176 (1998).
26. Yasuda, H. *et al.* Osteoclast differentiation factor is a ligand for osteoprotegerin/osteoclastogenesis-inhibitory factor and is identical to TRANCE/RANKL. *Proc Natl Acad Sci U S A* **95**, 3597-3602 (1998).
27. Xiong, J. *et al.* Matrix-embedded cells control osteoclast formation. *Nat Med* **17**, 1235-1241 (2011).
28. Fleisch, H. Bisphosphonates: mechanisms of action. *Endocr Rev* **19**, 80-100 (1998).
29. Hughes, D.E. *et al.* Bisphosphonates promote apoptosis in murine osteoclasts in vitro and in vivo. *J Bone Miner Res* **10**, 1478-1487 (1995).
30. Kodama, H. *et al.* Congenital osteoclast deficiency in osteopetrotic (op/op) mice is cured by injections of macrophage colony-stimulating factor. *J Exp Med* **173**, 269-272 (1991).
31. Marks, S.C., Jr. Morphological evidence of reduced bone resorption in osteopetrotic (op) mice. *Am J Anat* **163**, 157-167 (1982).
32. Vu, T.H. *et al.* MMP-9/gelatinase B is a key regulator of growth plate angiogenesis and apoptosis of hypertrophic chondrocytes. *Cell* **93**, 411-422 (1998).
33. Breur, G.J., VanEnkevort, B.A., Farnum, C.E. & Wilsman, N.J. Linear relationship between the volume of hypertrophic chondrocytes and the rate of longitudinal bone growth in growth plates. *J Orthop Res* **9**, 348-359 (1991).
34. Cooper, K.L. *et al.* Multiple phases of chondrocyte enlargement underlie differences in skeletal proportions. *Nature* **495**, 375-378 (2013).

35. Farnum, C.E., Tinsley, M. & Hermanson, J.W. Forelimb versus hindlimb skeletal development in the big brown bat, Eptesicus fuscus: functional divergence is reflected in chondrocytic performance in Autopodial growth plates. *Cells Tissues Organs* **187**, 35-47 (2008).
36. Wilsman, N.J., Bernardini, E.S., Leiferman, E., Noonan, K. & Farnum, C.E. Age and pattern of the onset of differential growth among growth plates in rats. *J Orthop Res* **26**, 1457-1465 (2008).
37. Wilsman, N.J., Farnum, C.E., Leiferman, E.M., Fry, M. & Barreto, C. Differential growth by growth plates as a function of multiple parameters of chondrocytic kinetics. *J Orthop Res* **14**, 927-936 (1996).
38. Marenzana, M. & Arnett, T.R. The Key Role of the Blood Supply to Bone. *Bone Res* **1**, 203-215 (2013).
39. Lee, S. *et al.* Intermittent PTH 1-34 administration improves the marrow microenvironment and endothelium-dependent vasodilation in bone arteries of aged rats. *J Appl Physiol (1985)* **124**, 1426-1437 (2018).
40. Kroll, M.H. Parathyroid hormone temporal effects on bone formation and resorption. *Bull Math Biol* **62**, 163-188 (2000).
41. Ferguson, C., Alpern, E., Miclau, T. & Helms, J.A. Does adult fracture repair recapitulate embryonic skeletal formation? *Mech Dev* **87**, 57-66 (1999).
42. Gerstenfeld, L.C. *et al.* Impaired fracture healing in the absence of TNF-alpha signaling: the role of TNF-alpha in endochondral cartilage resorption. *J Bone Miner Res* **18**, 1584-1592 (2003).
43. Goldring, M.B. Osteoarthritis and cartilage: the role of cytokines. *Curr Rheumatol Rep* **2**, 459-465 (2000).
44. Goldring, S.R. Pathogenesis of bone and cartilage destruction in rheumatoid arthritis. *Rheumatology (Oxford)* **42 Suppl 2**, ii11-16 (2003).
45. Carter, R.L. & Tanner, N.S. Local invasion by laryngeal carcinoma--the importance of focal (metaplastic) ossification within laryngeal cartilage. *Clin Otolaryngol Allied Sci* **4**, 283-290 (1979).
46. Castelijns, J.A. *et al.* Invasion of laryngeal cartilage by cancer: comparison of CT and MR imaging. *Radiology* **167**, 199-206 (1988).
47. Lubberts, E. *et al.* Treatment with a neutralizing anti-murine interleukin-17 antibody after the onset of collagen-induced arthritis reduces joint inflammation, cartilage destruction, and bone erosion. *Arthritis Rheum* **50**, 650-659 (2004).
48. Zwerina, J. *et al.* Single and combined inhibition of tumor necrosis factor, interleukin-1, and RANKL pathways in tumor necrosis factor-induced arthritis: effects on synovial inflammation, bone erosion, and cartilage destruction. *Arthritis Rheum* **50**, 277-290 (2004).
49. Takeshita, S., Kaji, K. & Kudo, A. Identification and characterization of the new osteoclast progenitor with macrophage phenotypes being able to differentiate into mature osteoclasts. *J Bone Miner Res* **15**, 1477-1488 (2000).
50. Xie, H. *et al.* PDGF-BB secreted by preosteoclasts induces angiogenesis during coupling with osteogenesis. *Nat Med* **20**, 1270-1278 (2014).
51. Maes, C. *et al.* Impaired angiogenesis and endochondral bone formation in mice lacking the vascular endothelial growth factor isoforms VEGF164 and VEGF188. *Mech Dev* **111**, 61-73 (2002).

## Methods Summary

### Wild type and Genetically Modified Mice

All wild-type bones were obtained from C57BL/6J mice from the specified age groups as mentioned in the text. For experiments involving wildtype mice, male mice were generally used compared to experiments involving transgenic animals where both male and females were used.

For lineage tracing experiments, *Csf1r*$^{Mer\text{-}iCre\text{-}Mer}$ mice[17] were bred with *Rosa26-tdTomato* reporter transgenic mouse line[18]. To induce Cre activity, tamoxifen (Sigma, T5648) was injected intraperitoneally at a dose of 12mg/kg per injection. For analysing embryonic stages, pregnant females were timed based on the presence of vaginal plug. A single injection of tamoxifen is supplemented with Progesterone (1mg/kg).

For inducible gene deletion experiments, Cre activity was induced by a tamoxifen dose of 80mg/kg which was provided in five consecutive daily injections from P10 to P14. For endothelial specific deletion experiments, *Cdh5(PAC)-CreERT2* transgenic mice[24] were bred with either conditional *Rankl*$^{lox/lox}$ mice[27] or conditional *Mmp9*$^{lox/lox}$ mice. For osteoclast specific deletions, *Csf1r*$^{Mer\text{-}iCre\text{-}Mer}$ mice were bred with conditional *Mmp9*$^{lox/lox}$ mice. Induced mice were humanely sacrificed to collect bones for analysis on P28.

Similarly, conditional *Dll4*$^{lox/lox}$ mice[52] and *Fbxw7*$^{lox/lox}$ mice[53] were bred with *Cdh5(PAC)-CreERT2* transgenic mice to induce endothelial specific gene deletions. In this case, a tamoxifen dose of 100mg/kg is provided in five consecutive daily injections from P36 to P40 and analysed on P54. For alendronate treatment on *Dll4* animals, 1mg/kg dose was injected three times a week for 4 weeks after tamoxifen injection and analysed on P70. Alendronate treatment on wildtype mice included a dose of 1mg/kg drug for 4 weeks before being euthanised. Similarly treated Dll4 mice were used for Parathyroid hormone (PTH)

experiment. In this experiment, daily subcutaneous injection of PTH (100ug/kg wt of mouse) was provided for 4 weeks after tamoxifen injection and analysed on P70.

For aged mice Vhl deletion experiment, *Vhl* $^{floxed/floxed}$ *Cdh5(PAC)-CreERT2*$^{T/+}$ mice were generated by breeding *Vhl* $^{floxed}$ mice[54] with *Cdh5(PAC)-CreERT2* mice. Cre negative *Vhl* $^{floxed/floxed}$ (control) and Cre positive *Vhl* $^{floxed/floxed}$ *Cdh5(PAC)-CreERT2*$^{T/+}$ (*Vhl* $^{i\Delta EC}$) mutant mice were used for the study. A two-time injection schedule with five injections in each schedule was followed to induce gene deletion in aged mice. Each schedule involved injection of 1,000 µg tamoxifen (Sigma, T5648) intraperitoneally every day for 5 days. Before second schedule, mice were rested for 16 days. Mice were again rested for 16 days after second schedule before being euthanised to collect femur and tibia for analysis.

Mice carrying osteopetrosis mutation (*op/op*) were purchased from Jackson laboratory (stock; 000231) for analysis. Homozygous animals showed impaired dental growth and a domed skull.

For Vegfr2 inhibitor treatment, SU5416 (Sigma, S8442) was administered intraperitoneally at 25mg/kg dose for five times from P10 and analysed on P28.

Control fluorescent liposome DiI and liposome clodronate suspensions were purchased from Liposoma, Amsterdam. The homogenous suspensions in PBS (5mg/ml) were mixed well before injecting in animals. For labelling macrophages, 100ul control fluorescent liposome DiI was injected intravenously and observed after 6, 24, 48 and 72 hrs. For depletion of VAOs, liposome clodronate was injected three times intravenously at 48hrs interval and analysed on 7days post first injection.

All animal experiments were performed in compliance with the local ethical and care guidelines at the Imperial College London and the International guidelines of the Home Office (UK). This study is compliant with all relevant ethical regulations regarding animal research.

**Immunohistochemistry Staining and Analysis**

Tibiae were collected by dissection from wild-type mice or mutant and control littermates and fixed immediately in 4% paraformaldehyde solution for 4 hrs on ice. Bones were decalcified with 0.5M EDTA with constant shaking at 4°C. Following decalcification, bones were kept for 24h in 20% (w/v) sucrose and 2% (w/v) polyvinylpyrrolidine (PVP) solution. Prior to cryosectioning, bones were embedded in 8% (w/v) gelatin, 20% (w/v) sucrose, 2% PVP. Bone sections were generated using a Leica 3050S cryostat on microscopic slides and allowed to air-dry. The detailed protocol was published earlier[55].

For immunostaining and phenotypic analyses, bone sections were hydrated, permeabilised with 0.25% Triton-X for 10 min, blocked with 5% donkey serum (blocking solution) for 30 min and incubated with primary antibodies diluted in blocking solution for 2.5 hrs at RT or overnight at 4°C. Primary antibodies used: Endomucin (Santa Cruz, 1:100), Tartate resistant alkaline phosphatase (TRAP) (Thermo Scientific, 1:100), Integrin beta 3 (Cell Signalling, 1:100), V-type proton pump-3 (abcam, 1:100), Collagen-X (abcam, 1:100), CD31 (R&D systems, 1:100), CD68 (Abcam, 1:200), Receptor activator of nuclear factor κ-B (RANK) (R&D systems, 1:100), Cathepsin K (abcam 1:100), Chloride voltage-gated channel 7 (Clcn7) (abcam 1:100), Osteopontin (R&D systems, 1:200), Osterix (abcam 1:200), MMP13 (abcam 1:200) Nrp1 (R&D systems, 1:100), Tie2 (R&D systems, 1:100), CD45 (BD pharmigen, 1:100) and SOX9 (R&D systems, 1:400) and cleaved caspase-3 (cell signalling, 1:200).

Following primary antibody staining, slides were washed with PBS, three times, 5 mins each and incubated with the relevant Alexa Fluor-conjugated secondary antibodies for 1 hr at RT. Secondary antibodies used: Anti-rat Alexa Fluor 594 (Invitrogen; A21209, 1:400), anti-rabbit Alexa Fluor 546 (Invitrogen; A11035, 1:400), anti-goat Alexa Fluor 488

(Invitrogen; A11055, 1:400), anti-goat Alexa Fluor 647 (Invitrogen; A21447, 1:400) and DAPI for nuclear staining. Sections were washed with PBS thoroughly and then mounted with FluoroMount-G solution (Southern Biotech) and sealed with coverslips.

High resolution immunofluorescent images were acquired using a Leica TCS SP8 confocal laser scanning microscope.

**TUNEL Assay**

Bones were processed as above and 25 µm sections were generated using the cryostat. TUNEL (Sigma-Aldrich 11767305001) assay was performed as per manufacturer's guidelines. Briefly, TUNEL labelling was performed after immunostaining protocol. The reaction mixture was prepared by mixing 5ul TUNEL enzyme with 45ul TUNEL label buffer per sample and incubated for 60min at 37$^{o}$C in a humidified chamber in the dark. Slides were washed three times with PBS, mounted and imaged using Leica SP8 confocal laser scanning microscope.

**EdU Labelling**

For EdU labelling of proliferating cells, we injected mice with 300 µg EdU (Invitrogen) intraperitoneally and were subjected to euthanasia 3 hours after the injection. Bones were collected immediately and processed following the protocol described earlier. The bone cryosections were immunostained for EdU using Click-iT chemistry following the manufacturer's protocols (Invitrogen).

**Flow cytometry**

C57Bl/6 wildtype mice were used for isolating osteoclasts. We generally collected bones from both femur and tibia of two or more animals. Bones were dissected and cleaned

of all adhering muscle and crushed with a mortar and pestle in ice-cold PBS. RBC lysis was performed on total bone marrow cells to deplete erythrocytes. Further collagenase digestion was performed for 30 min at 37°C. Cells were then washed and filtered to obtain a single cell suspension.

Cells were stained with anti-RANK-PE (Invitrogen 1:50) for 1hr on ice followed by labelling with Vybrant Dye Cycle (Thermofisher Scientific) for 30 mins at 37°C. Cells were either analysed using LSR II or sorted using Aria III (BD Biosciences) with FACSDiva software. Total RANK+ cells were gated for separating the cells further on the basis of their nuclear content using Vybrant dye. In general, we sorted 2-nucleated cells for VAO and 4 (or more) nucleated cells for BAO subset.

CD31 and Endomucin FACS immune-staining was performed following the protocol published earlier[14].

**Irradiation and Transplantation assay**

For irradiation experiments, wild type C57BL/6J mice of 8 weeks old were sub-lethally irradiated at 650rads. The double transgenic *Csf1r*$^{Mer\text{-}iCre\text{-}Mer}$ with *Rosa26-tdTomato* reporter mouse line were used for labelling cells. Sorted Tomato+ VAO and BAO subset of purified $5x10^4$ osteoclasts were transplanted intravenously into irradiated mice along with wildtype bone marrow cells. Transplanted mice were sacrificed after 7 days and bones were analysed for the presence of Tomato+ cells. BAO subset did not survive transplantation as Tomato+ cells were not observed in the transplanted mice.

**Quantitative RT-PCR**

Cells were sorted directly into lysis buffer of the RNeasy Plus Micro Kit (QIAGEN). Total RNA was isolated as per manufacturer's guidelines. 100 ng of DNA/reaction was used

for cDNA synthesis using the iScript cDNA Synthesis System (Bio-Rad). qPCR was performed using PowerUp SYBR Green Real-Time PCR Master Mix with customised primer pairs. Sequences of primer pairs used in the study could be provided upon request. All gene expression assays were normalised to endogenous *Actb* levels.

**Image Processing and Quantification**

Z-stacks of images were 3D-reconstructed and analysed using Imaris Image Analysis Software (version 9.0). ImageJ, Adobe Illustrator and Adobe Photoshop were used to process images in compliance with the Cell's guidelines for processing digital images. IMARIS and ImageJ were used for all quantifications.

*Quantification of osteoclasts:* Number of osteoclasts were manually quantified on high resolution images using IMARIS and ImageJ software. Mono- or bi- nucleated osteoclast structures present in close association with blood vessels were considered as VAOs and large multinucleated (>4) cells present on the bone surface were considered as BAOs. For quantifying number of nuclei, high resolution z-stack images of osteoclasts were visualised at multiple planes to count number of nuclear structures in the cell. Similarly, sizes of osteoclasts were measured along the length of their interaction with either blood vessels or bone.

*Growth plate size:* For quantifying growth plate sizes, distance between blood vessel front in the metaphysis and secondary ossification centre were measured. Mouse tibia were used in general for all the growth plate measurements.

*Anastomosing bulges:* For quantification of bulges involved in anastomoses, bulges in the leading front of the tibial bone vasculature were analysed. Bulges in close association and/or in contact with the adjacent bulges are considered as anastomosing. Single planes of Z-stack images were examined to understand the interaction of bulges.

*Angular orientations:* Alignment measurements were calculated based on proximal and distal axis of bone. Multiple longitudinal bone sections were used to measure direction of blood vessels and chondrocytes. For chondrocytes, direction of their differentiation axis towards hypertrophic chondrocytes was used. For secondary ossification centres, both proximal and distal axis from longitudinal sections and radial axis from transverse sections were used. ImageJ was used to draw axis along invading blood vessels and chondrocyte stacks. The angle of incidence was measured between the proximal distal axis of bone and the respective axis of type-H vessels, chondrocytes and type-L vessels.

**RNA sequencing**

Cells were sorted in flow cytometry and total RNA was isolated following the protocol mentioned earlier.

*Library preparation:* RNA quality was checked using a 2100 BioAnalyzer (Agilent), and multiple samples were pooled to form 2 independent replicates and proceeded for library preparations. Libraries were prepared with TruSeq Total RNA Library Preparation Kit (Illumina) following the manufacturer's guidelines. Sequencing of libraries was carried out at LMS Genomic facility on Illumina HiSeq 2500 platform with 100nt length paired-end reads. The sequencing data have been deposited to Array Express database (https://www.ebi.ac.uk/arrayexpress/) with the accession number E-MTAB-6857.

*Data quality:* The quality assessment of raw sequence data of BAO and VAO samples were performed by FastQC (Version: FastQC 0.11.5, (http://www.bioinformatics. babraham.ac.uk/projects/fastqc/). No samples were discarded from the analysis.

*Alignment to reference genome:* The raw reads were mapped to genome assembly of mouse (GRCm38) using subread with setting the parameter (Version: subread-1.5.3; [subread-align -T 16 -t 0 -i -r -R -o]). The mouse genome was downloaded from https:// www.ensembl.org

and the mouse genome index was created from subread-build command from subread tool[56]. The quantification of aligned reads on a per gene basis was obtained using HTSeq with the following settings (Version: HTSeq- 0.9.1; [htseq-count-mode = intersection-nonempty−stranded = reverse])[57]. To explore similarities and dissimilarities between the samples, count data were normalized using the Variance Stabilizing Transformation (VST) function from the DESeq2 package[58]. Differential gene expression analysis between VAO and BAO was performed using DESeq2. The significant differentially expressed genes are selected (coding biotype) with FDR-adjusted P value cutoff < 0.05. Ensembl IDs were annotated to gene symbols and Entrez Gene using biomaRt (BioConductor version, 3.4.1). The differentially regulated genes list is provided in supplementary table-1.

**Statistics and Reproducibility**

GraphPad Prism software was used for all calculations. Biological parameters are shown as mean ± standard deviation and numerical data as mean ± standard error of the mean. Unless otherwise stated, two-tailed student's *t*-tests were used to determine statistical significance. $p < 0.05$ was considered statistically significant. In others, regular two-way ANOVA was performed along with Bonferroni's multiple comparison tests to assess statistical significance with a 95% confidence interval. Confocal images presented in the figures are one representative biological replicate of an experiment. Multiple, independent experiments were performed to validate the reproducibility of experimental data, as indicated in the respective figure legends. RNA-Seq experiment/ analysis was performed once. Two samples indicated in the RNA-Seq are osteoclasts isolated from 5 animals in each set. For volcano plot, adjusted p-values obtained from nbinomWaldTest comparing BAO and VAO. Experimental mice were not excluded from any analysis, and no randomisation or blinding was used. Sample sizes were chosen with experience from prior experiments. Several bone/tissue samples per

mouse were included in the analysis of the following figure panels - Figure 3b,c,e; 4b,c,f; Supplementary Figure 3c; 4b; 6b,d,e,f,h, and derived the statistics from the average of all combined samples per animal.

## Data Availability

RNA–seq data that support the findings of this study have been deposited in the Array Express database under accession code E-MTAB-6857.

Numerical source data giving rise to graphical representations and statistical descriptions have been provided as Supplementary Table 2. All other data supporting the findings of this study are available from the corresponding author on reasonable request.

## Methods References


52. Koch, U. *et al.* Delta-like 4 is the essential, nonredundant ligand for Notch1 during thymic T cell lineage commitment. *J Exp Med* **205**, 2515-2523 (2008).
53. Hoeck, J.D. *et al.* Fbw7 controls neural stem cell differentiation and progenitor apoptosis via Notch and c-Jun. *Nat Neurosci* **13**, 1365-1372 (2010).
54. Haase, V.H., Glickman, J.N., Socolovsky, M. & Jaenisch, R. Vascular tumors in livers with targeted inactivation of the von Hippel-Lindau tumor suppressor. *Proc Natl Acad Sci U S A* **98**, 1583-1588 (2001).
55. Kusumbe, A.P., Ramasamy, S.K., Starsichova, A. & Adams, R.H. Sample preparation for high-resolution 3D confocal imaging of mouse skeletal tissue. *Nat Protoc* **10**, 1904-1914 (2015).
56. Liao, Y., Smyth, G.K. & Shi, W. The Subread aligner: fast, accurate and scalable read mapping by seed-and-vote. *Nucleic Acids Res **41***, e108 (2013).
57. Anders, S., Pyl, P.T. & Huber, W. HTSeq--a Python framework to work with high-throughput sequencing data. *Bioinformatics* **31**, 166-169 (2015).
58. Love, M.I., Huber, W. & Anders, S. Moderated estimation of fold change and dispersion for RNA-seq data with DESeq2. *Genome Biol* **15**, 550 (2014).

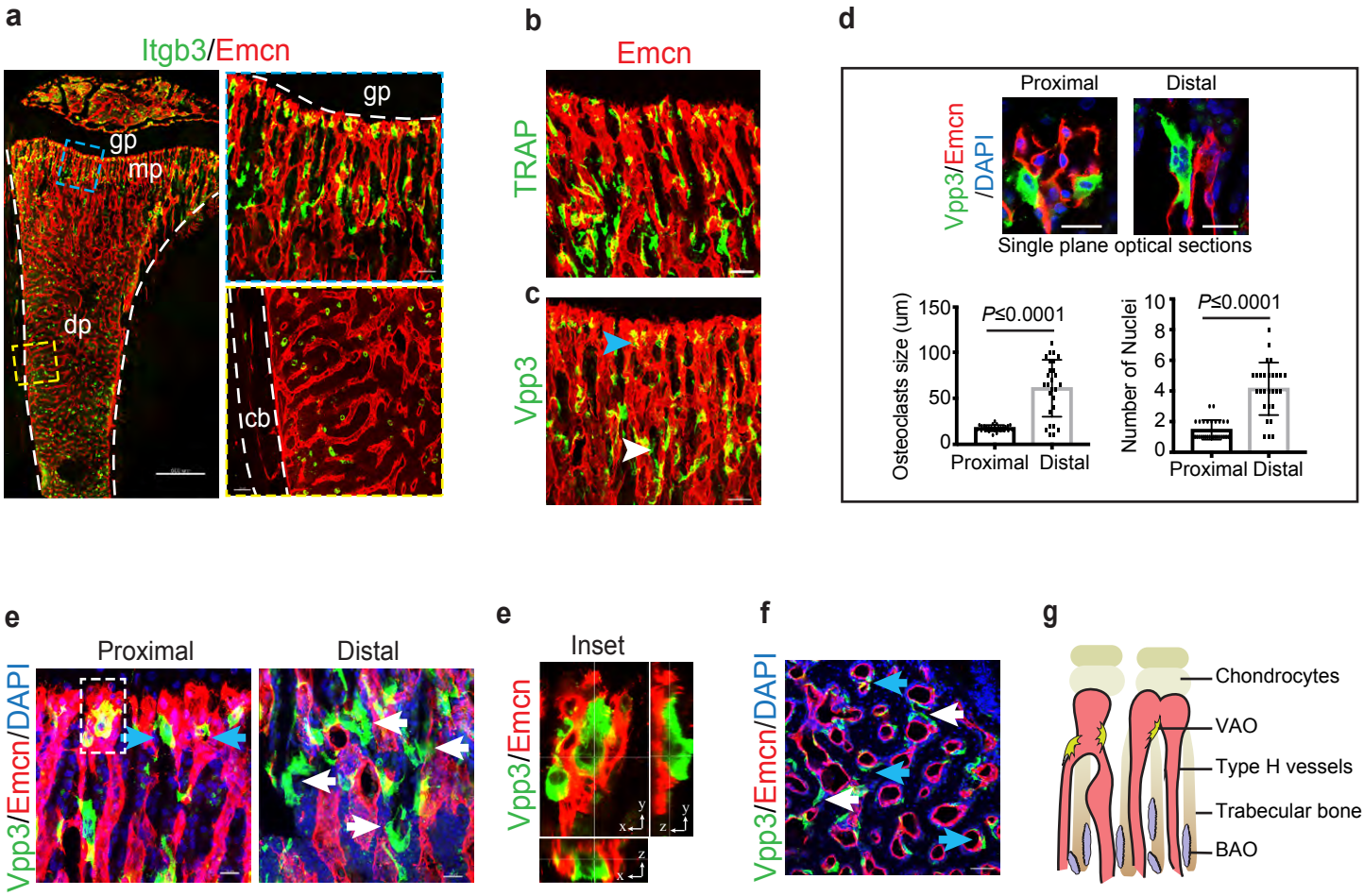


Romeo et al., Fig. 1

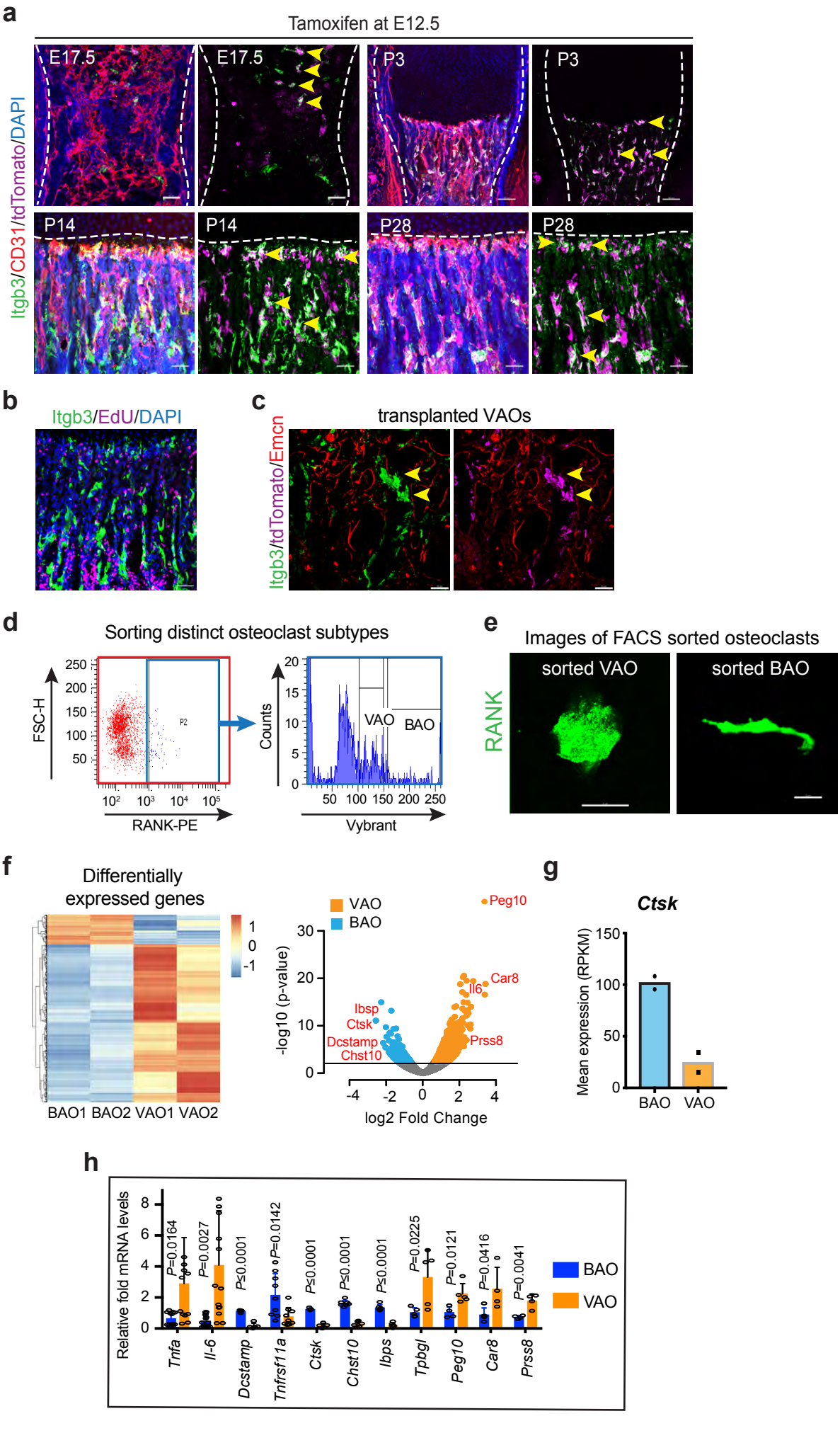


Romeo et al., Fig. 2

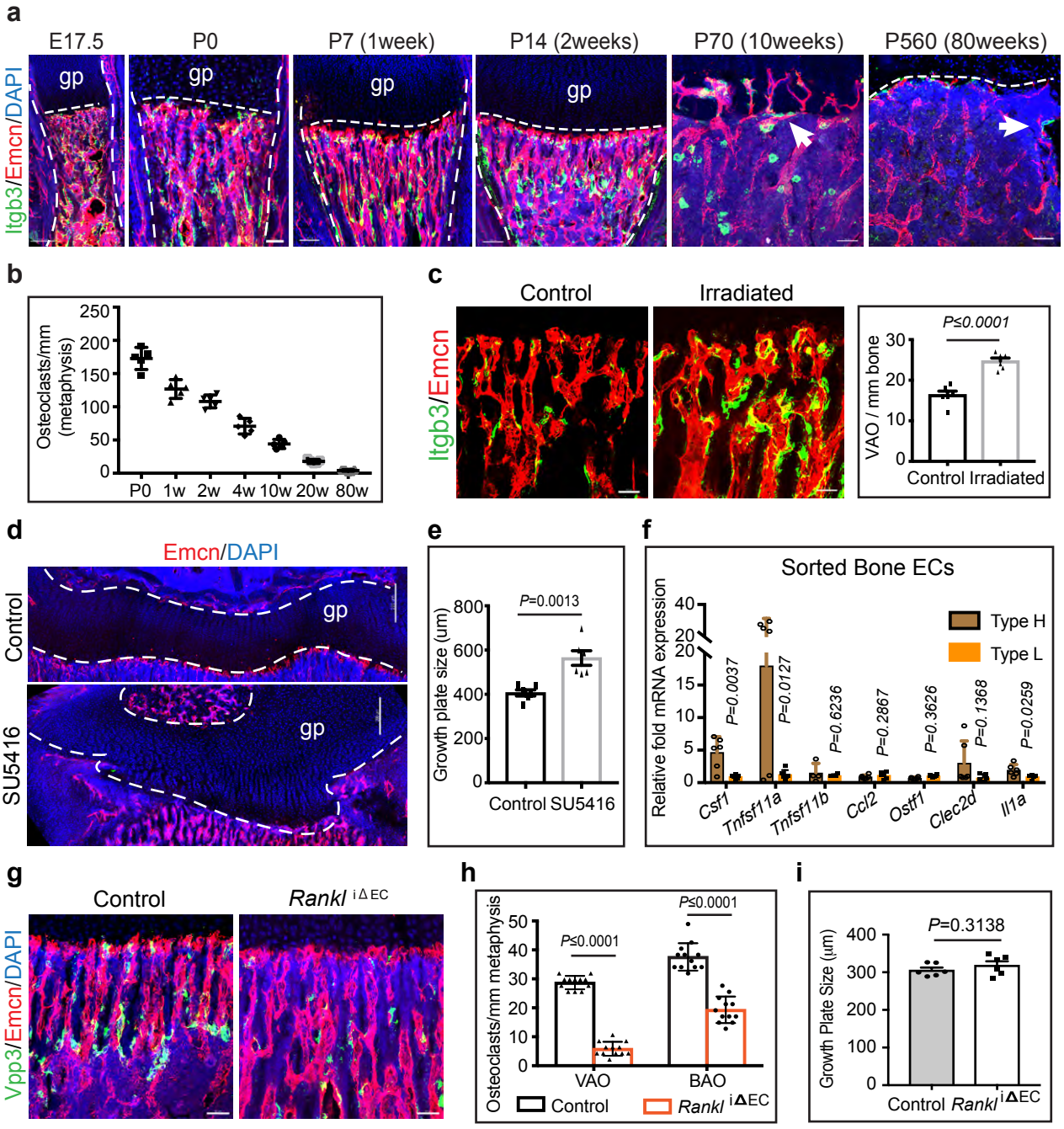


Romeo et al., Fig. 3

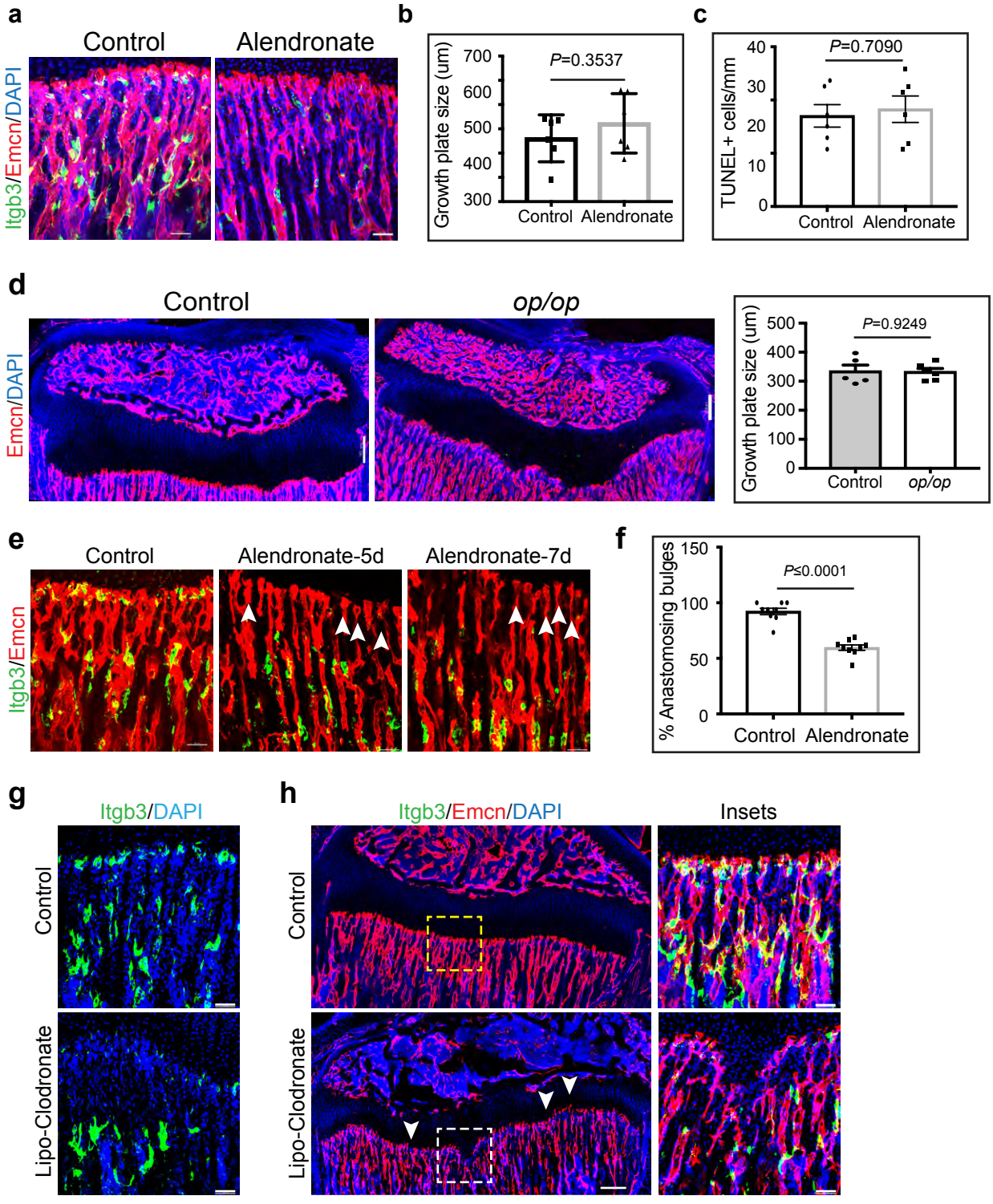


Romeo et al., Fig. 4

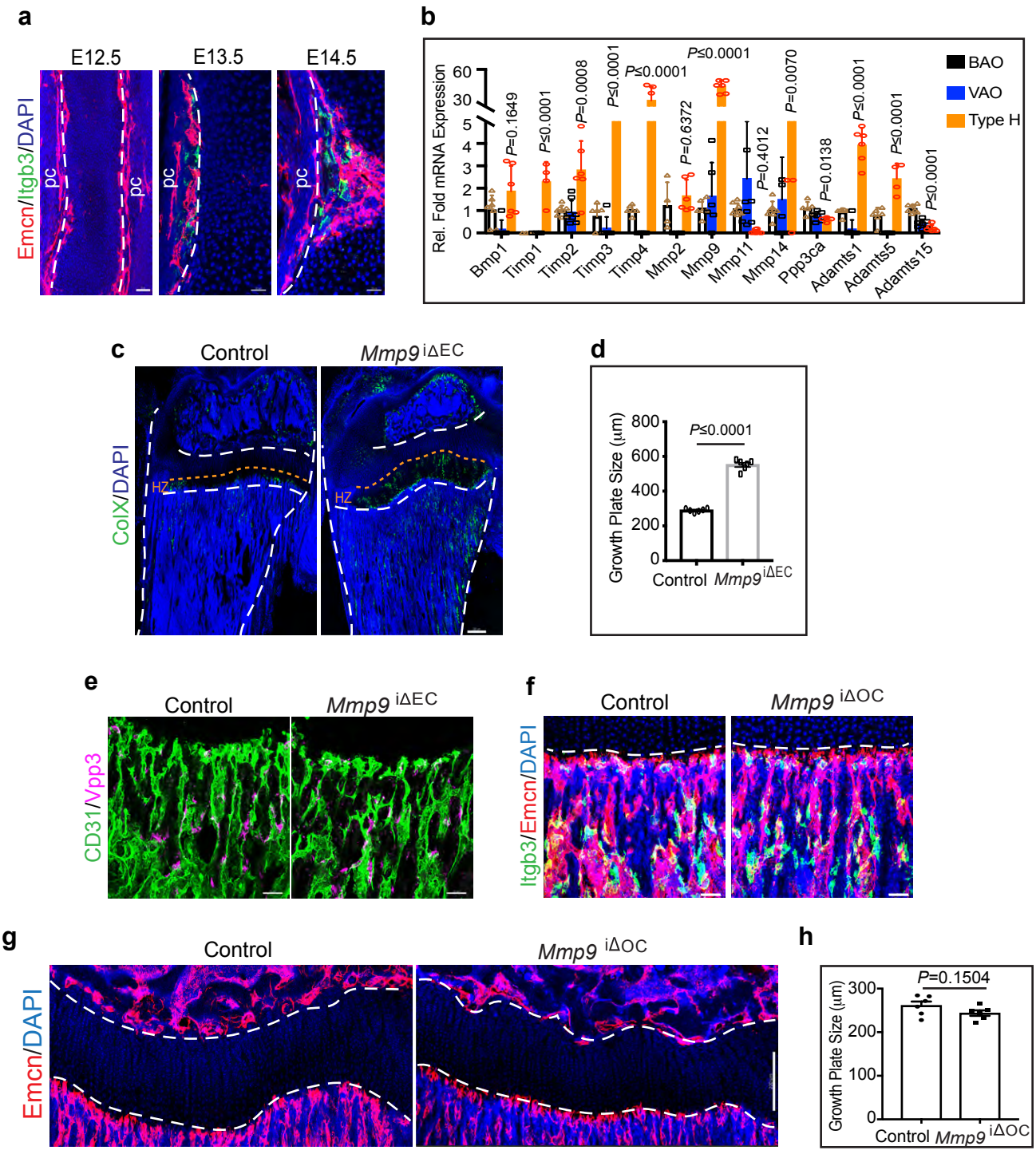


Romeo et al., Fig. 5

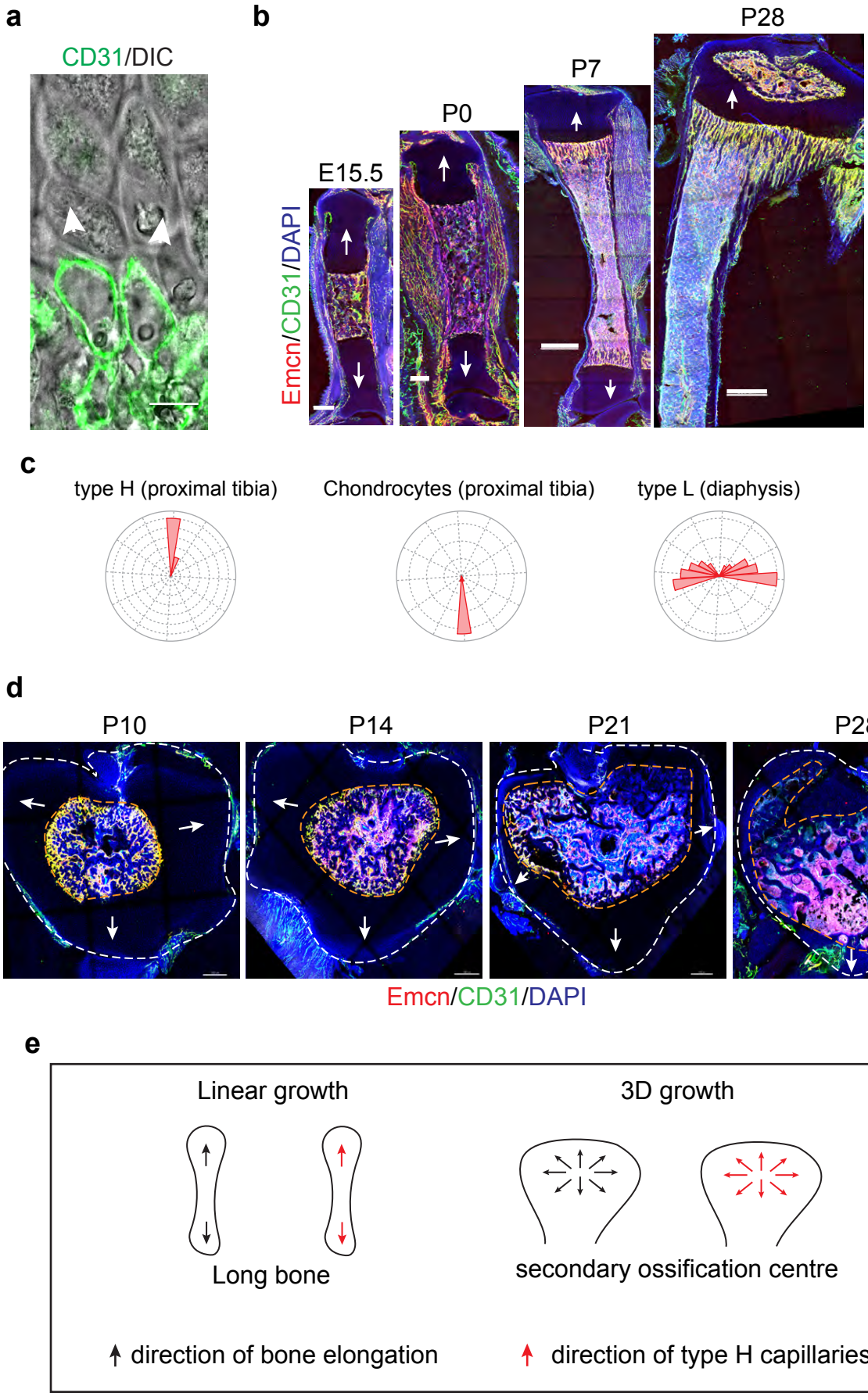


Romeo et al., Fig. 6

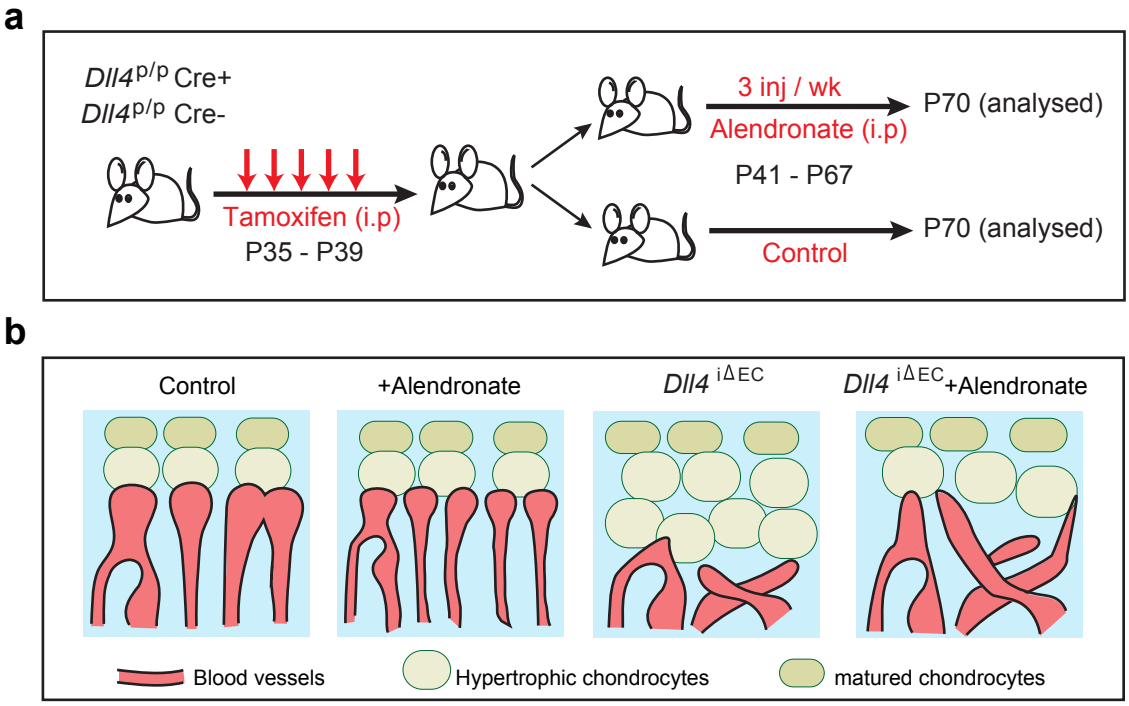


Romeo et al., Fig. 7

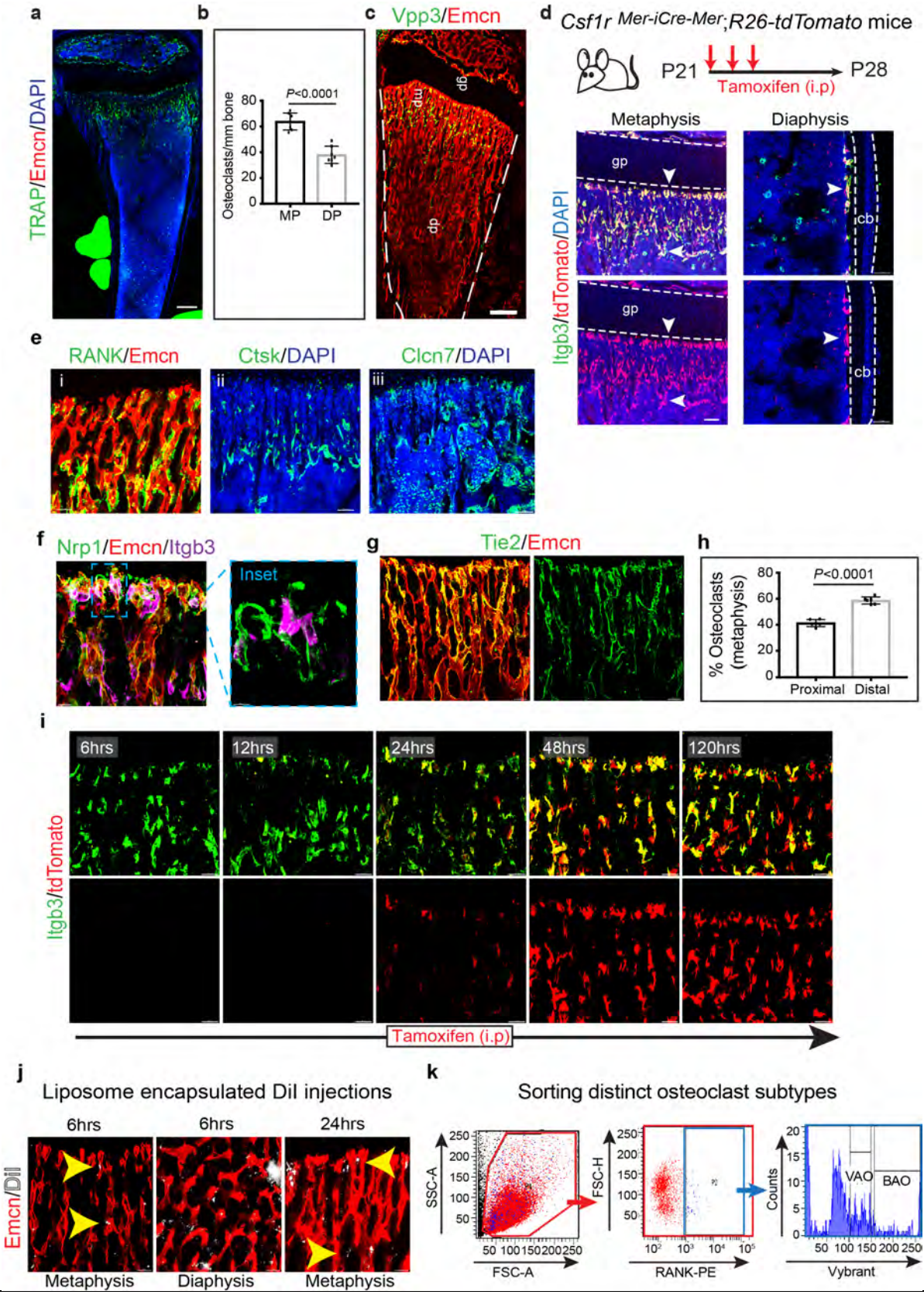
a
TRAP/Emcn/DAPI
b
Osteoclasts/mm bone
P<0.0001
MP
DP
c
Vpp3/Emcn
mp
dp
d
Csf1r Mer-iCre-Mer;R26-tdTomato mice
P21
Tamoxifen (i.p)
P28
Metaphysis
Diaphysis
Itgb3/tdTomato/DAPI
gp
cb
e
RANK/Emcn
Ctsk/DAPI
Clcn7/DAPI
i
ii
iii
f
Nrp1/Emcn/Itgb3
Inset
g
Tie2/Emcn
h
% Osteoclasts (metaphysis)
P<0.0001
Proximal
Distal
i
6hrs
12hrs
24hrs
48hrs
120hrs
Itgb3/tdTomato
Tamoxifen (i.p)
j
Liposome encapsulated DiI injections
6hrs
6hrs
24hrs
Emcn/DiI
Metaphysis
Diaphysis
Metaphysis
k
Sorting distinct osteoclast subtypes
SSC-A
FSC-A
FSC-H
RANK-PE
Counts
VAO
BAO
Vybrant

**Supplementary Figure 1**

Osteoclast subtypes in bone

**a,** Tile scan image shows localisation of osteoclasts in a 4 weeks old mouse tibia. TRAP (osteoclasts, green) immunostaining indicates the distribution of osteoclasts in this postnatal bone. DAPI is nuclear counterstain. Scale bar, 500μm. Representative image from 3 repeated experiments.
**b,** Quantification of total osteoclasts present in tibia of a 4-week old mouse. MP, metaphysis; DP, diaphysis. Data represent mean ± sem from n=7 biologically independent samples. *P* values, two-tailed unpaired *t*-tests.
**c,** Tile scan shows distribution of Vpp3+ osteoclasts (green) in a 4-weeks old mouse tibia from 8 repeated experiments. Blood vessels were immunostained with Endomucin (Emcn, red). mp, metaphysis; dp, diaphysis. Scale bar, 300μm
**d,** Tibia from double transgenic mice generated using *Csf1r* $^{Mer\text{-}iCre\text{-}Mer}$ and *R26-tdTomato* were analysed for Tomato expression after tamoxifen induction. Experimental schedule of tamoxifen injection and analysis are as shown. Tomato$^{+}$ large cells present in the metaphysis and diaphysis coincides with the osteoclasts markers expression in mouse tibia as observed from 10 repeated experiments. Scale bar, 100μm (metaphysis), 50μm (diaphysis).
**e,** Osteoclast markers expression in 4 weeks old mouse tibia. RANK (green) and Emcn (red) immunostaining in (**i)**, Cathepsin K (green) and DAPI (blue) in (**ii)**, and Chloride voltage gated channel-7 (green) and DAPI (blue) in (**iii)** show similar distribution pattern of osteoclasts in the metaphysis of tibia. Endomucin (Emcn) marks blood vessels. DAPI is nuclear counterstain. Representative images from 4 repeated experiments. Scale bar, 50μm
**f-g,** Pro-angiogenic macrophage markers expression in leading vascular front. **f**, Neuropilin1 (Nrp1, green) is not found to be expressed in osteoclasts (Itgb3, magenta). **g**, Tie2 (green) expression is detected only in blood vessels in the metaphysis. Emcn (red) labels blood vessels. Representative images from 4 repeated experiments. Scale bars, 50μm, inset 8μm.
**h,** Graph shows percentage of osteoclasts occupying proximal and distal metaphysis of 3 weeks old mouse tibia. Data represent mean ± sem from n=6 biologically independent samples. *P* values, two-tailed unpaired *t*-tests.
**i,** A single low-dose tamoxifen injection to genetically label and understand relation between VAO and BAO subsets using double transgenic *Csf1r* $^{Mer\text{-}iCre\text{-}Mer}$ and *R26-tdTomato* mice. Tomato expression (red) was analysed after 6, 12, 24, 48 and 120hrs post induction. Itgb3 immunostaining (green) was performed to label osteoclasts. Scale bar, 50μm. Representative images from 3 repeated experiments.
**j,** Liposome encapsulated DiI dye injection showed localisation of DiI in phagocytes and a few cells in the metaphysis by 6hrs. Both VAO and BAO subsets were labelled by 24hrs. Blood vessels (Emcn, red); Phagocytic cells (Liposome DiI, White). Scale bar, 50μm. Representative images from 4 repeated experiments.
**k,** Representative flow cytometry plots demonstrate the gating strategy used to purify osteoclasts from erythrocytes-lysed total bone cells. First, RANK+ cells were gated out from total bone marrow cells. Then these cells were further separated on the basis of their nuclear content i.e cells with 2 nuclei were separated as VAO population compared cells BAO subset having >4 nuclei.

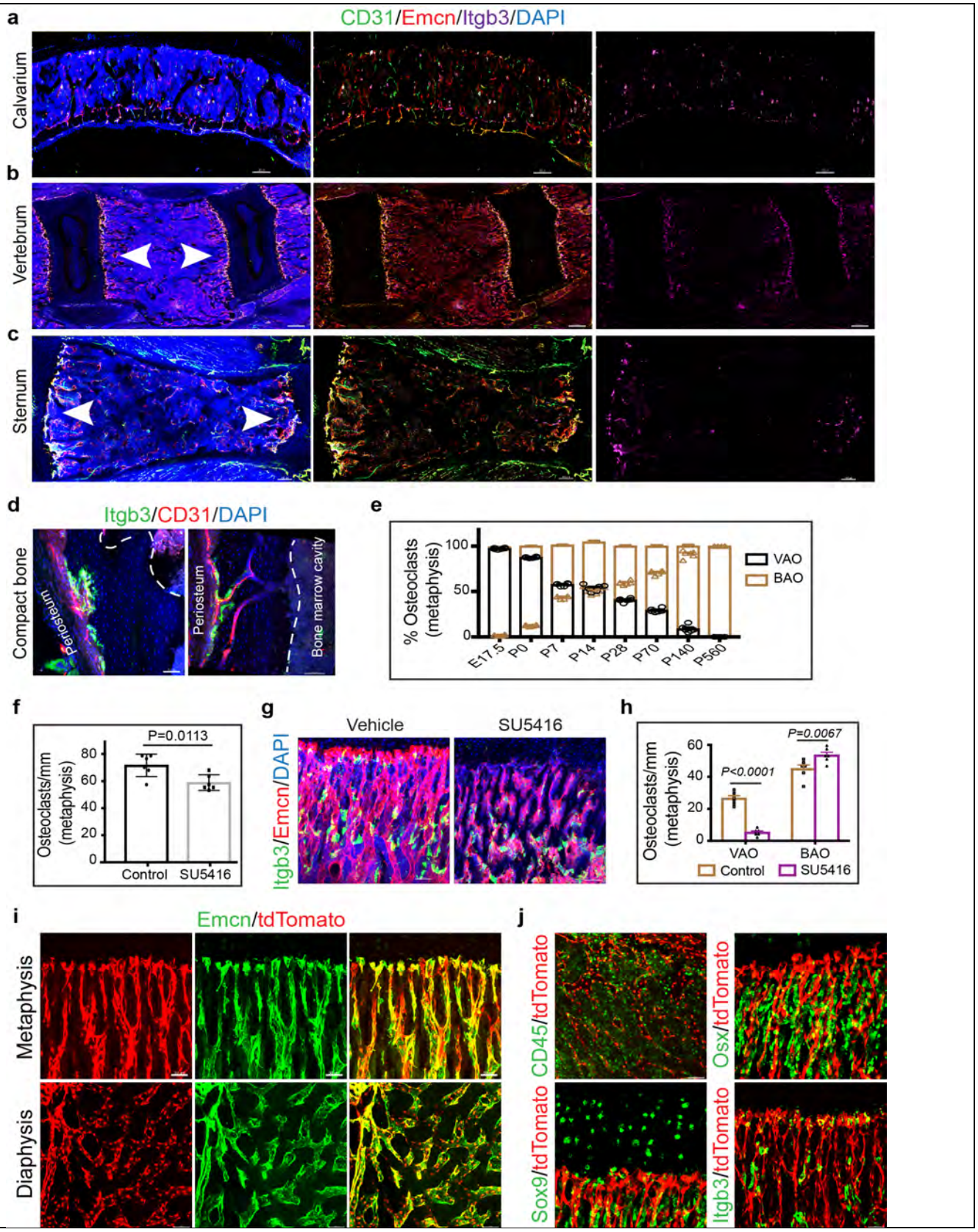
a
CD31/Emcn/Itgb3/DAPI
Calvarium
b
Vertebrum
c
Sternum
d
Itgb3/CD31/DAPI
Compact bone
Periosteum
Periosteum
Bone marrow cavity
e
% Osteoclasts (metaphysis)
100
50
0
VAO
BAO
E17.5
P0
P7
P14
P28
P70
P140
P560
f
Osteoclasts/mm (metaphysis)
P=0.0113
80
60
40
20
0
Control
SU5416
g
Vehicle
SU5416
Itgb3/Emcn/DAPI
h
Osteoclasts/mm (metaphysis)
P=0.0067
P<0.0001
60
40
20
0
VAO
BAO
Control
SU5416
i
Emcn/tdTomato
Metaphysis
Diaphysis
j
CD45/tdTomato
Osx/tdTomato
Sox9/tdTomato
Itgb3/tdTomato

**Supplementary Figure 2**

Distribution of osteoclasts and their association with blood vessels

**a-c,** Tile scan images show distribution of osteoclasts (Itgb3, magenta) in various bone tissues such as calvarium (**a**), Vertebrum (**b**) and sternum (**c**) of 4-week-old mice. Blood vessels were immunostained using endomucin (Emcn, red) and CD31(green). DAPI stains nuclei. Scale bars, 200μm (a,b), 100μm (c). Representative images from 3 repeated experiments.

**d,** Osteoclasts (Itgb3, green) in the cortical region of tibia are large elongated structures similar to BAO. Despite their proximity to blood vessels (Emcn, red), they seem to stretch along the bone surface. Scale bar, 50μm. Representative images from 8 repeated experiments.

**e,** Graph shows percentage variation of BAO and VAO subsets during bone growth. Developing bone contains predominantly VAO subset which decreases with age that lead to majority of BAO subset in adults. Data represent mean ± sem from n=6 animals pooled from 3 experiments.

**f**, Quantification of total osteoclasts number in the tibial metaphysis of control and vegfr2 inhibitor (SU5416) treated mice. Data represent mean ± sem from n=6 biologically independent samples. *P* values, two-tailed unpaired *t*-tests.

**g,** Confocal images showing metaphysis of control and Vegfr2 inhibitor (SU5416) treated mouse tibia immunostained for blood vessels (Emcn, red) and osteoclasts (Itgb3, green) at 4 weeks of age. Scale bar, 50μm. Representative images from 6 experimental animals.

**h,** Vegfr2 treatment resulted in dramatic reduction in percentage of VAO subset. Data represent mean ± sem from n=6 biologically independent samples pooled from 4 experiments. *P* values, two way-ANOVA with Sidak's multiple comparisons test.

**i-j,** Tibia from double transgenic mice generated using *Cdh5 (PAC) CreERT2* and *R26 lox-STOP-lox tdTomato* transgenic background were analysed for Tomato expression after tamoxifen induction. Tamoxifen induces tomato expression in cells which undergo Cre mediated recombination. Thick bone sections were analysed for tomato expression and immunostained for various cell markers to understand the specificity of the Cre driver. **i,** Confocal images show blood vessel specific recombination in metaphysis and diaphysis of bone. Endomucin immunostaining (emcn, green) coincides with the endogenous tomato expression (red). **j,** Confocal images show Tomato expression (red) along with other cell type specific markers; CD45 labels haematopoietic cells, Osterix (Osx) marks osteoprogenitors, Sox9 was used to label chondrocytes and Itgb3 shows distribution of osteoclasts. Tomato expression does not overlap with any of these cell types. This also indicates the specificity of this Cre driver for blood vessels in bone. Scale bar, 50μm. Representative images from 10 repeated experiments.

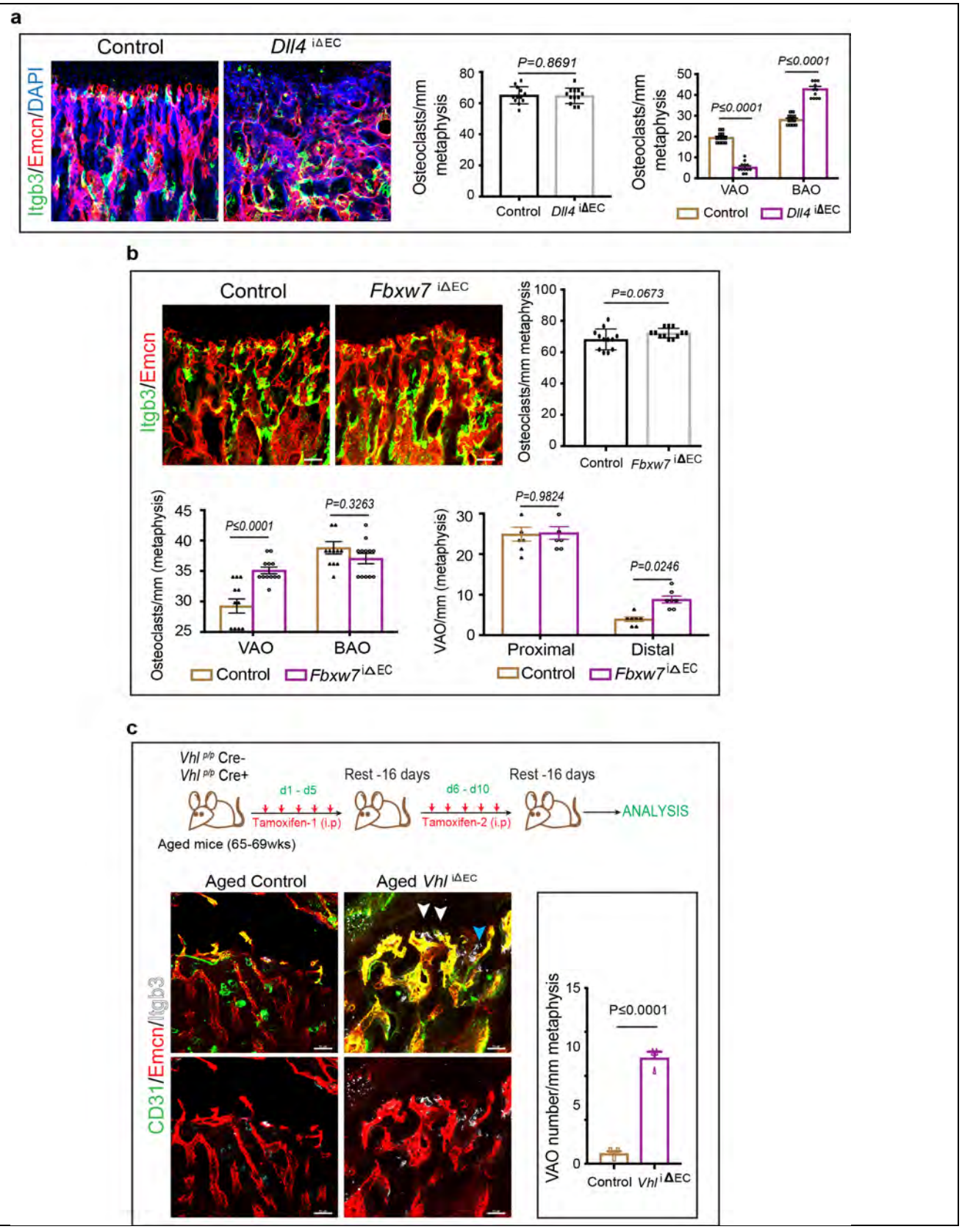
a
Control
Dll4 iΔEC
Itgb3/Emcn/DAPI
Osteoclasts/mm metaphysis
P=0.8691
Control
Dll4 iΔEC
P≤0.0001
P≤0.0001
VAO
BAO
Control
Dll4 iΔEC
b
Control
Fbxw7 iΔEC
Itgb3/Emcn
Osteoclasts/mm metaphysis
P=0.0673
Control
Fbxw7 iΔEC
Osteoclasts/mm (metaphysis)
P≤0.0001
P=0.3263
VAO
BAO
Control
Fbxw7iΔEC
VAO/mm (metaphysis)
P=0.9824
P=0.0246
Proximal
Distal
Control
Fbxw7iΔEC
c
Vhl p/p Cre-
Vhl p/p Cre+
d1 - d5
Tamoxifen-1 (i.p)
Rest -16 days
d6 - d10
Tamoxifen-2 (i.p)
Rest -16 days
ANALYSIS
Aged mice (65-69wks)
Aged Control
Aged Vhl iΔEC
CD31/Emcn/Itgb3
VAO number/mm metaphysis
P≤0.0001
Control
Vhl iΔEC

**Supplementary Figure 3**

Type-H vessels support VAO subtype of osteoclasts

**a,** Representative images show arrangement of blood vessels (Emcn, red) and osteoclasts (Itgb3, green) in the metaphysis of 5-week-old *Dll4* $^{i\Delta EC}$ mutants and control littermates from n=4 independent experiments. Dapi, Nuclei. Scale bar, 50μm. Graphs show osteoclasts number in *Dll4* $^{i\Delta EC}$ mutants and their littermate controls. Total number of osteoclasts is not affected in endothelial specific deletion of *Dll4*. Data represent mean ± sem from n=12 animals pooled from 4 independent experiments. *P* values, two-tailed unpaired *t*-tests. However, quantification of VAO and BAO osteoclast subtypes in the metaphysis of *Dll4* $^{i\Delta EC}$ mutants and their control littermates shows reduction in ECs coordinated with the decline in VAO and increase in BAO subtypes. Data represent mean ± sem from n=12 animals pooled from 4 independent experiments. *P* values, two way-ANOVA with Sidak's multiple comparisons test.

**b,** Representative confocal images showing arrangement of blood vessels (Emcn, red) and osteoclasts (Itgb3, green) in the metaphysis of *Fbxw7* $^{i\Delta EC}$ mutants and their littermate controls from 4 independent experiments. Scale bar, 50μm. Quantification of total osteoclasts shows similar number in *Fbxw7* $^{i\Delta EC}$ mutants and their littermate controls. Data represent mean ± sem from n=12 animals pooled from 4 independent experiments. *P* values, two-tailed unpaired *t*-tests. However, Quantification of VAO and BAO osteoclast subtypes in the metaphysis of *Fbxw7* $^{i\Delta EC}$ mutants and their control littermates show increase in VAO subset upon promotion of ECs in *Fbxw7* $^{i\Delta EC}$ animals. Data represent mean ± sem from n=12 animals pooled from 4 independent experiments. *P* values, two way-ANOVA with Sidak's multiple comparisons test. Quantification of VAO subset indicates the increase in VAO is prominent in the distal metaphysis. Data represent mean ± sem from n=7 samples pooled from 4 independent experiments. *P* values, two way-ANOVA with Sidak's multiple comparisons test.

**c**, Experimental scheme shows tamoxifen injection schedule used to induce gene deletion in aged *Vhl* mice. Representative confocal images show reactivation of type-H vessels (yellow) in *Vhl* $^{i\Delta EC}$ mutants compared to their aged control littermates (*Vhl* $^{p/p}$ Cre-) from n=3 independent animals. Type-H vessels show high expression of endothelial markers CD31 (green) and Emcn (red). Reactivation of type-H vessels is associated with increase in osteoclasts (Itgb3, white) in the metaphysis. White arrows indicate osteoclasts in close association with type-H vessels while blue arrow indicates an osteoclast not associated with blood vessels. Scale bar, 50μm. Quantification of blood vessel associated osteoclasts (VAOs) show increase in their number in *Vhl* $^{i\Delta EC}$ mutants compared to their aged control littermates. Data represent mean ± sem from n=3 biologically independent experiments. *P* values, two-tailed unpaired *t*-tests.

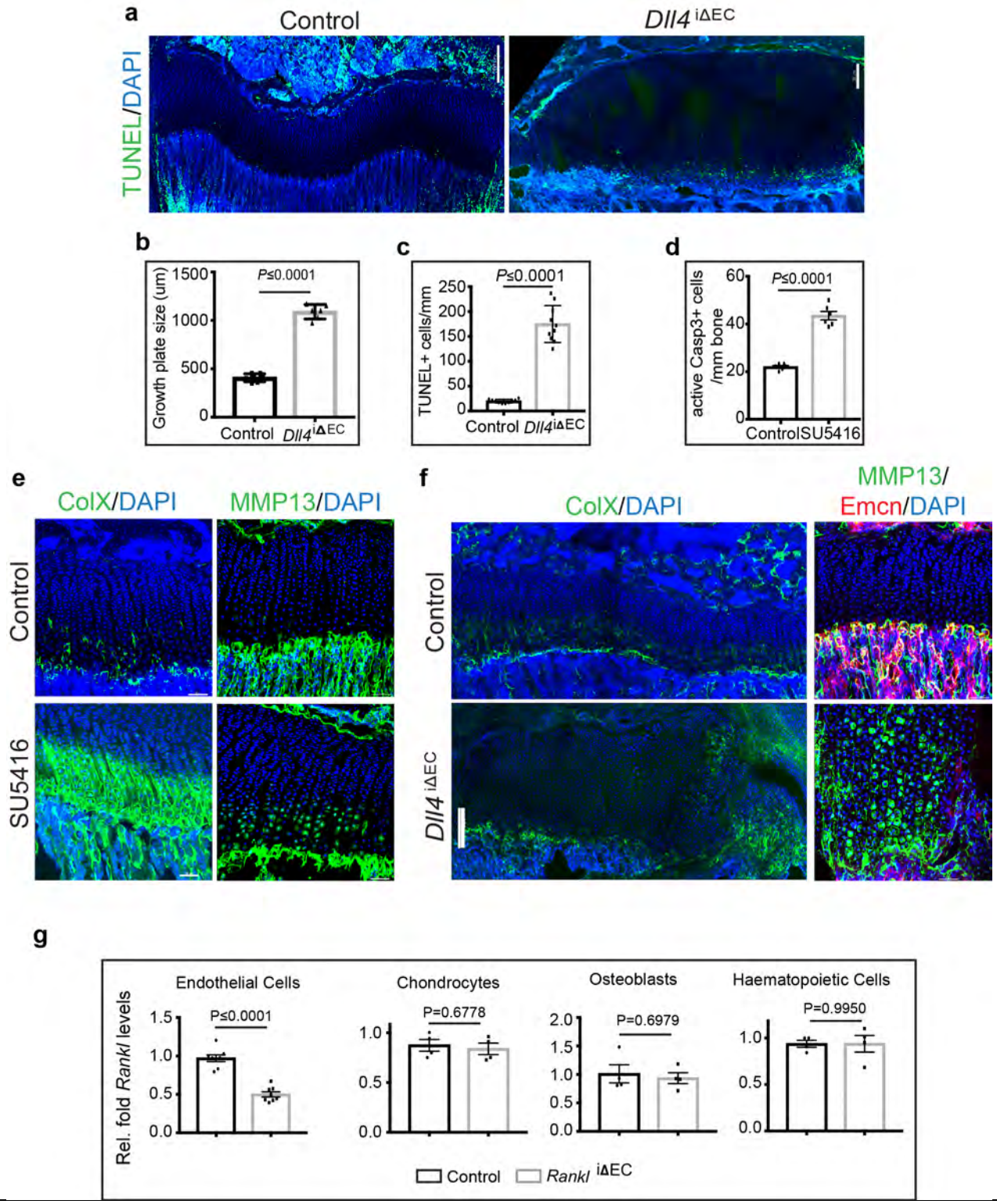


**Supplementary Figure 4**

Growth plate analysis upon defective blood vessel growth

**a,** Tile scan images show TUNEL+ cells (green) in the growth plates of *Dll4* $^{i\Delta EC}$ mutants and their littermate controls of 10-weeks old. DAPI is nuclear counterstain. Scale bars, 200μm. Representative image from 6 biologically repeated experiments.
**b,** Graph shows growth plate sizes of endothelial *Dll4* mutants and their littermate controls. Data represent mean ± sem from n=6 biologically independent experiments. *P* values, two-tailed unpaired *t*-tests.
**c,** Quantification of TUNEL+ cells in the growth plate region of *Dll4* $^{i\Delta EC}$ and corresponding controls show increase in TUNEL+ cells in the mutant animals, Data represent mean ± sem from n=10 bones pooled from 4 experiments. *P* values, two-tailed unpaired *t*-tests.
**d,** Quantification of cleaved caspase3+ cells in control and vegfr2 inhibitor (SU5416) treated mice. Data represent mean ± sem from n=6 biologically independent experiments. *P* values, two-tailed unpaired *t*-tests.
**e,** Representative images show Collagen-X and MMP13 expression in the growth plates of 4-week-old control and Vegfr2 inhibitor (SU5416) treated mice from 6 biologically independent animals. Scale bars, 50μm.
**f,** Tile scan image show Collagen-X (ColX, green) expression in the growth plates of *Dll4* $^{i\Delta EC}$ mutants and littermate controls. Scale bars, 150μm. Maximum intensity projection images show MMP13 (green) and Endomucin (red) in the growth plates of *Dll4* $^{i\Delta EC}$ mutants and littermate controls. Scale bars, 50μm. DAPI stains nuclei. Both are representative images from 6 biologically independent animals.
**g,** Graphs show Rankl transcript levels in various cell types in both *Rankl* $^{i\Delta EC}$ mutants and their littermate controls. Total RNA isolated from purified endothelial cells of n=8 biologically independent animals, chondrocytes of n=4 biologically independent animals, osteoblasts/osteocytes of n=4 biologically independent animals and haematopoietic cells of n=4 biologically independent animals were subjected to reverse transcription and quantitative PCR to analyse *Rankl* levels. Significant decrease in Rankl transcripts were observed in bone endothelial cells while other cell types did not show any change. This confirms the endothelial specific deletion of *Rankl* in these mutants. Data represent mean ± sem. *P* values, two-tailed unpaired *t*-tests.

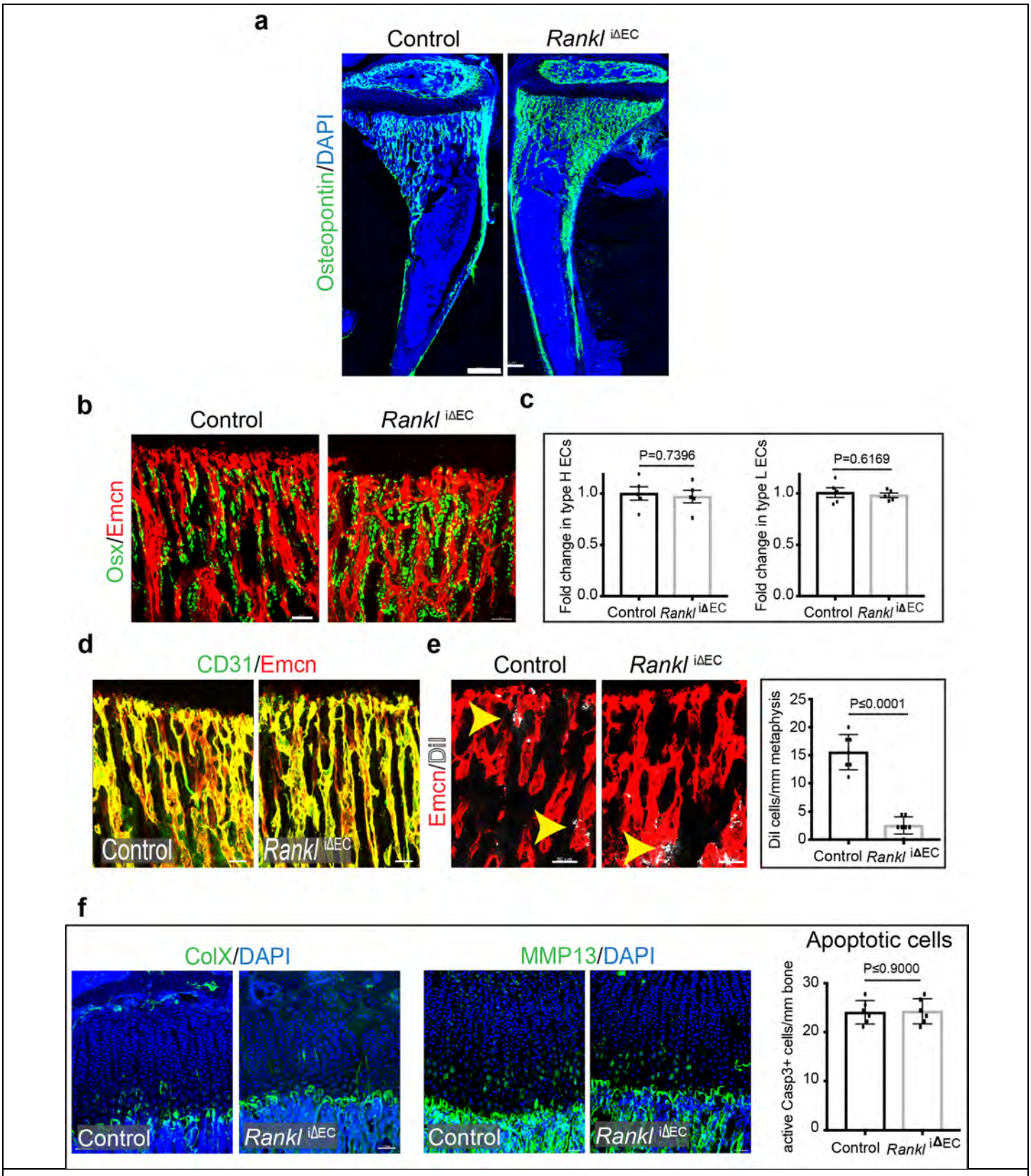


**Supplementary Figure 5**

Interaction between blood vessels and osteoclasts

**a,** Tile scan images of *Rankl* $^{i\Delta EC}$ mutant and littermate control mice tibia immunostained for Osteopontin (green) display increased bone matrix in the mutant animals. DAPI is nuclear counterstain. Scale bars, 500μm. Representative images from 4 biologically independent animals.

**b,** Confocal image of *Rankl* $^{i\Delta EC}$ mutant and littermate control mice tibial metaphysis show distribution of osteoprogenitors (Osx, green). Blood vessels were immunostained with Emcn (red). Scale bars, 50μm. Representative images from 6 biologically independent animals.

**c,** Graphs show quantification of fold change in number of type-H ($CD31^{high}$/$Emcn^{high}$) and type-L ($CD31^{low}$/$Emcn^{low}$) endothelial cells in *Rankl* $^{i\Delta EC}$ mutants and their littermate controls on P28. Data represent mean ± sem from n=5 biologically independent animals. *P* values, two-tailed unpaired *t*-tests.

**d,** Confocal images of *Rankl* $^{i\Delta EC}$ mutants and their littermate control mice show status of type-H endothelial cells in 4 weeks old tibia. Type-H endothelial cells were identified using high expression of CD31 (green) and Emcn (red) markers. Scale bars, 50μm. Representative images from 6 biologically independent animals.

**e,** Liposome encapsulated DiI dye injection showed localisation of phagocytic cells in tibia of *Rankl* $^{i\Delta EC}$ mutants and their littermate controls after 24hrs post-injection. Both VAO and BAO subsets were labelled in control mice. Reduced VAO number in *Rankl* $^{i\Delta EC}$ mutants led to decreased DiI labelling in proximal metaphysis. Blood vessels (Emcn, red); Phagocytic cells (Liposome DiI, White). Scale bars, 50μm. Representative images from 3 biologically independent animals. Quantification of DiI labelled cells indicate decreased phagocytic cells in the proximal metaphysis of *Rankl* $^{i\Delta EC}$ mutants. Data represent mean ± sd from n=7 biologically independent animals. *P* values, two-tailed unpaired *t*-tests.

**f,** Confocal images show growth plates of *Rankl* $^{i\Delta EC}$ mutant and littermate control mice tibia immunostained for Collagen-X and MMP13 (green). DAPI stains nucleus. Hypertrophic zone in the growth plate is not affected in the mutant animals. Scale bars, 50μm. Representative images from n=3 biologically independent animals. Quantification of cleaved caspase3+ cells in *Rankl* $^{i\Delta EC}$ mutant and littermate control mice. Data represent mean ± sd from n=6 biologically independent animals. *P* values, two-tailed unpaired *t*-tests.

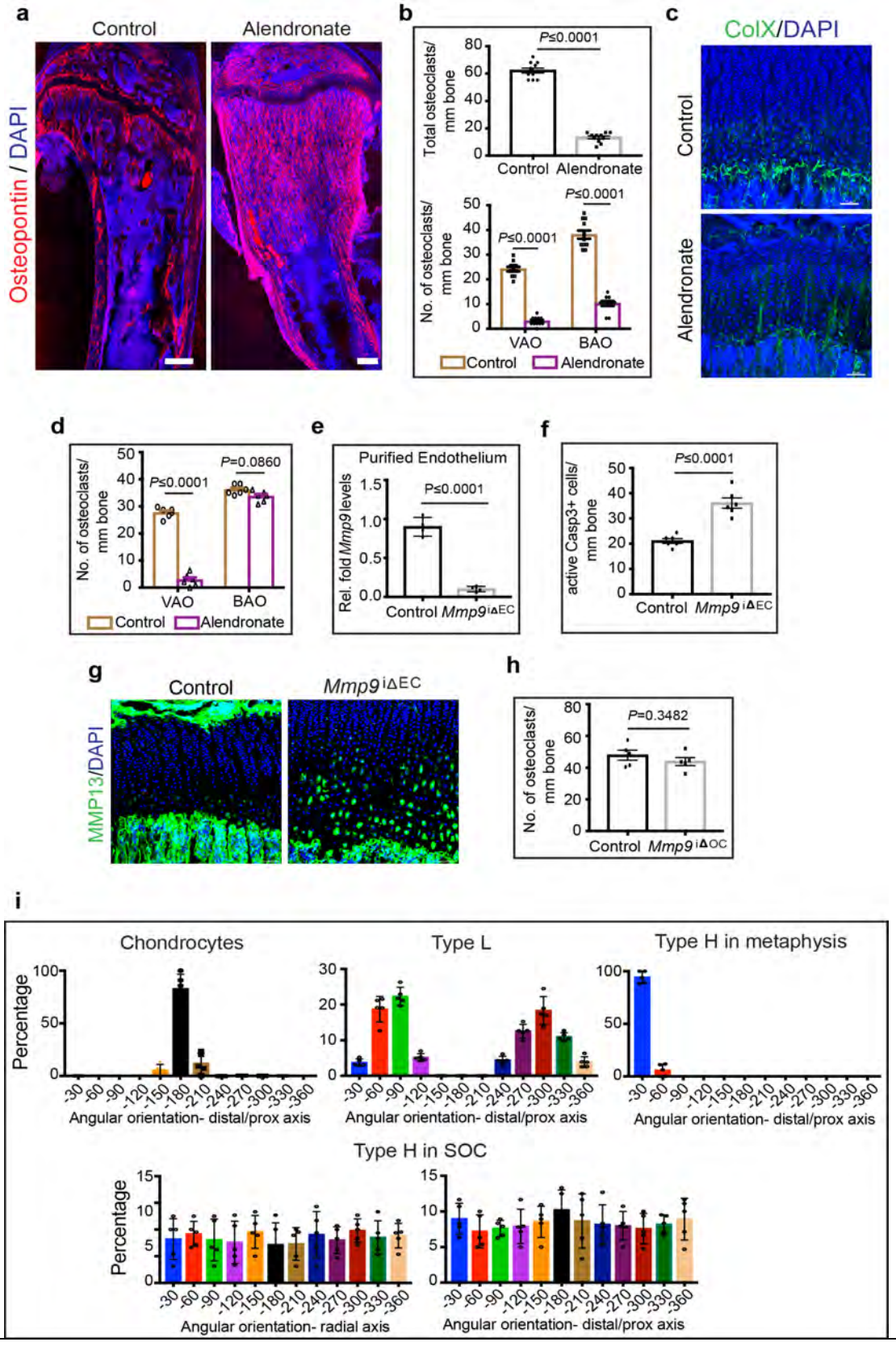
a
Control
Alendronate
Osteopontin / DAPI
b
Total osteoclasts/ mm bone
P≤0.0001
Control
Alendronate
No. of osteoclasts/ mm bone
P≤0.0001
P≤0.0001
VAO
BAO
Control
Alendronate
c
ColX/DAPI
Control
Alendronate
d
No. of osteoclasts/ mm bone
P≤0.0001
P=0.0860
VAO
BAO
Control
Alendronate
e
Purified Endothelium
Rel. fold Mmp9 levels
P≤0.0001
Control
Mmp9 iΔEC
f
active Casp3+ cells/ mm bone
P≤0.0001
Control
Mmp9 iΔEC
g
Control
Mmp9 iΔEC
MMP13/DAPI
h
No. of osteoclasts/ mm bone
P=0.3482
Control
Mmp9 iΔOC
i
Chondrocytes
Type L
Type H in metaphysis
Percentage
Angular orientation- distal/prox axis
Type H in SOC
Angular orientation- radial axis
Angular orientation- distal/prox axis

**Supplementary Figure 6**

Growth plate analysis and blood vessel orientations in bone

**a,** Tile scan images immunostained for Osteopontin (red) indicate increased bone formation in the alendronate treated animals compared to their control. DAPI is nuclear counterstain. Scale bars, 500μm (control), 300μm (alendronate). Representative images from 4 repeated experiments.
**b,** Quantification of osteoclasts show reduced number in the alendronate treated animals in comparison to their controls. Data represent mean ± sem from n=11 animals pooled from 4 independent experiments. *P* values, two-tailed unpaired *t*-tests. Further quantifying both VAO and BAO subsets indicate that alendronate treatment affects both the subtypes. Data represent mean ± sem from n=11 animals pooled from 4 independent experiments. *P* values, two way-ANOVA with Sidak's multiple comparisons test.
**c,** Confocal images of Collagen-X (ColX, green) immunostained growth plates in control and alendronate treated animals show unaffected hypertrophic zones. DAPI is nuclear counterstain. Scale bars, 50μm. Representative images from 3 repeated experiments.
**d,** Quantification of osteoclasts number in tibia after short-term treatment of alendronate. Alendronate administration at 7th day shows reduction in VAO subtypes while BAO subtypes were not significantly affected by the treatment. Data represent mean ± sem from n=6 biologically independent animals. *P* values, two way-ANOVA with Sidak's multiple comparisons test.
**e,** Graph showing Mmp9 transcript levels in purified endothelial cells of *Mmp9* $^{i\Delta EC}$ mutants and their littermate controls indicates reduction of *Mmp9* levels after endothelial specific deletion. Data represent mean ± sd from n=4 biologically independent experiments. *P* values, two-tailed unpaired *t*-tests.
**f,** Quantification of cleaved caspase3+ cells in control and *Mmp9* $^{i\Delta EC}$ mutants indicate increase in activated caspase3+ cells upon endothelial specific deletion of *Mmp9*. Data represent mean ± sem from n=6 biologically independent experiments. *P* values, two-tailed unpaired *t*-tests.
**g,** Confocal images show growth plates of *Mmp9* $^{i\Delta EC}$ mutant and littermate control mice tibia immunostained for MMP13 (green). DAPI stains nucleus. Scale bars, 50μm. Representative images from 4 repeated experiments.
**h,** Quantification of osteoclasts show a comparable number in osteoclast specific *Mmp9* deletion mutants in comparison to their littermate controls. Data represent mean ± sd from n=5 animals pooled from 2 experiments. *P* values, two-tailed unpaired *t*-tests.
**i,** Quantifications to show direction of type-H and type-L vessels and chondrocytes in bone. Percentage of blood vessel structures and columnar chondrocytes were plotted based on their angular orientation along the distal-proximal axis of tibia. Angular orientation of blood vessel structures in secondary ossification centre (SOC) were measured along the radial axis of bone transverse sections. In long bones. type-H vessels are arranged along the direction of bone growth while columnar chondrocytes in growth plate expand in parallelly opposite direction. Type-L vessels are generally in perpendicular orientation. In SOCs, type-H vessels do not show any particular orientation and their broad orientations indicate their growth in all the directions. Data represent mean ± sd from n=5 biologically independent samples. *P* values, two-tailed unpaired *t*-tests.

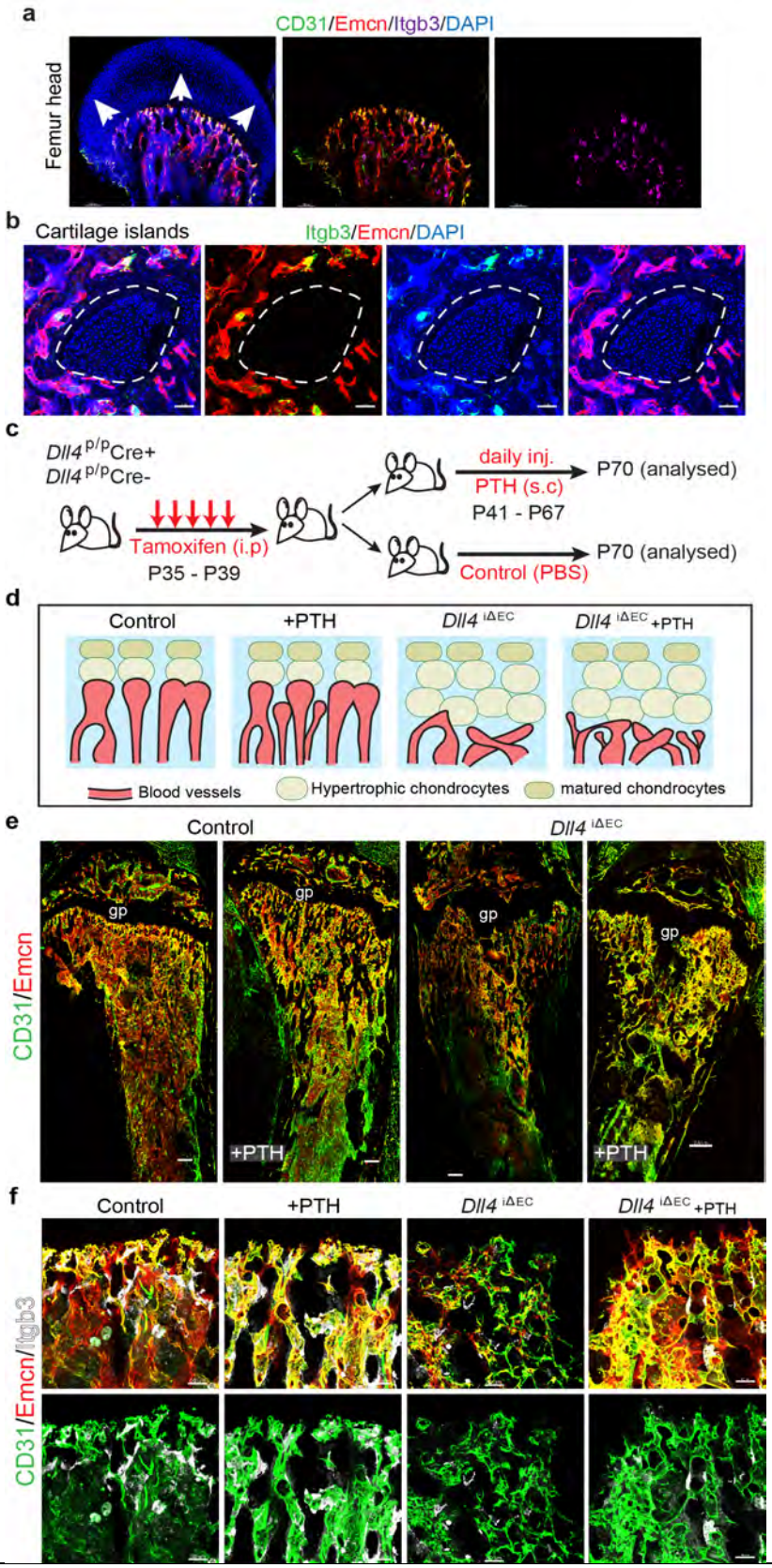
a
CD31/Emcn/Itgb3/DAPI
Femur head
b
Cartilage islands
Itgb3/Emcn/DAPI
c
Dll4 p/p Cre+
Dll4 p/p Cre-
Tamoxifen (i.p)
P35 - P39
daily inj.
PTH (s.c)
P41 - P67
P70 (analysed)
P70 (analysed)
Control (PBS)
d
Control
+PTH
Dll4 iΔEC
Dll4 iΔEC +PTH
Blood vessels
Hypertrophic chondrocytes
matured chondrocytes
e
Control
Dll4 iΔEC
CD31/Emcn
gp
+PTH
f
Control
+PTH
Dll4 iΔEC
Dll4 iΔEC +PTH
CD31/Emcn/Itgb3
CD31/Emcn

**Supplementary Figure 7**

Relation between blood vessel orientation and bone growth

**a,** Tile scan confocal image illustrates type-H vessels arrangement in femur head. Type-H vessels identified by CD31 (green) and Emcn (red) high expression is localised near cartilage region. White arrows indicate the direction of blood vessel growth. Osteoclasts (Itgb3, magenta) show similar distribution pattern as observed in tibia. DAPI is nuclei counterstain. Scale bars, 100μm. Representative image from 2 repeated experiments.
**b,** Confocal images show cartilage islands formed in *Dll4* $^{i\Delta EC}$ mutants treated with alendronate caused by growth of randomly directed blood vessels. Itgb3, osteoclasts (green); Emcn, blood capillaries (red); DAPI, Nuclei (blue). Scale bars, 50μm. Representative images from 4 repeated experiments.
**c,** Experimental scheme illustrating the tamoxifen administration and PTH treatment in *Dll4* transgenic animals to investigate their function in blood vessels and directional bone growth.
**d,** Schematic illustration highlighting the behaviour of type-H capillaries in each treatment conditions that first misdirect and then promote blood vessel growth.
**e,** Confocal tile scan images show status and distribution of type-H blood vessels (yellow) identified by CD31 (green) and Endomucin (Emcn, red) high expression in 10-weeks old *Dll4* $^{i\Delta EC}$ mutants and littermate control mice treated with PTH. Orientation of bone in the treated conditions is not affected. gp, growth plate. Scale bars, 300μm. Representative images from 3 repeated experiments.
**f,** Maximum intensity projections of mouse tibial metaphysis immunostained for Endomucin (red), CD31 (green) and Itgb3 (white) to label blood capillaries and osteoclasts. PTH treatment promotes bone and blood vessel formation and does not inhibit osteoclasts in control mice. *Dll4* $^{i\Delta EC}$ mutants show defective blood vessel growth. PTH treatment in *Dll4* $^{i\Delta EC}$ mutants promoted local blood vessel growth. Scale bars, 50μm. Representative images from 3 repeated experiments.

Appended as separate excel file

**Supplementary Table 1**

Differentially expressed genes between VAO and BAO subsets.

The complete list of 950 differentially expressed genes between VAO and BAO (FDR-adjusted *P* value cutoff <0.05 with coding biotype). Differentially expressed genes were calculated using negative binomial Wald function and p-values were adjusted using Benjamin-Hochberg method. Cells sorted from 5 independent experiments were pooled into 2 samples for RNAseq.

Appended as separate excel file

**Supplementary Table 2**

Statistical source data

The excel file contains numerical source data of all the graphical representations in the figures and their statistical analysis.

Appended as separate excel file

**Supplementary Table 3**

Primer sequences

The complete list of primer sequences used in this study for various quantitative PCR analysis.